# A Small Tau Fragment Specifically Templates Four Repeat Tau Aggregates Through Multiple Generations

Andrew P. Longhini[1,2], Austin Dubose[3], Samuel Lobo[4], Vishnu Vijayan[3], Yeran Bai[1,2,5], Erica Keane Rivera[1,2], Julia Salar-Jarque[1,2], Arina Nikitina[1,2], Daniel C. Carrettiero[1,2,6], Matthew Unger[1,2], Olivia Sclafani[1,2], Valerie Fu[1,2], Michael Vigers[3], Luc Buee[7,8], Isabelle Landrieu[9,10] Scott Shell[4], Joan E. Shea[3,11], Songi Han[3,4,12], Kenneth S. Kosik[1,2,12,*]

[1] Neuroscience Research Institute, University of California Santa Barbara, Santa Barbara, California, USA.
[2] Molecular, Cell and Developmental Biology, University of California Santa Barbara, Santa Barbara, California, USA.
[3] Department of Chemistry and Biochemistry, University of California Santa Barbara, Santa Barbara, California, USA.
[4] Department of Chemical Engineering, University of California Santa Barbara, Santa Barbara, California, USA.
[5] Photothermal Spectroscopy Corp., Santa Barbara, CA 93101, USA
[6] Center for Natural and Human Sciences, Federal University of ABC, São Bernardo do Campo, SP, Brazil.
[7] Univ. Lille, Inserm, CHU Lille, LilNCog – Lille Neuroscience & Cognition, F-59000 Lille, France.
[8] LabEx DISTALZ, Alzheimer & Tauopathies Team, F-59000 Lille, France.
[9] CNRS EMR9002 – BSI - Integrative Structural Biology F-59000 Lille, France
[11] Univ. Lille, Inserm, CHU Lille, Institut Pasteur de Lille, U1167 - RID-AGE - Risk Factors and Molecular Determinants of Aging-Related Diseases, F-59000 Lille, France.
Department of Physics, University of California, Santa Barbara, Santa Barbara, CA.
[12] Lead Contacts
* Correspondence: kosik@lifesci.ucsb.edu (K.S.K.)

## Summary

Prion-like spread of disease-specific tau conformers is a hallmark of all tauopathies. We used a 19-residue probe peptide spanning the R2/R3 splice junction of tau to induce aggregation specifically of 4R, but not 3R tau. The aggregates can propagate as isoform-specific seeds over multiple generations, have a high β-sheet content, a lipid signal, and resemble the PSP cryo-EM fold. A simulation of peptide free energy landscapes pinpointed the features of the hairpin structure uniquely found in the cryo-EM structures of pure 4R tauopathies and captured in the peptide. These molecular dynamic simulations were experimentally validated by the S305K substitution in 4R tau, corresponding to the position found in 3R tau. This single amino acid substitution prevented tau aggregates induced by the prion-like probe peptide. The tau aggregates were dynamic and displayed growth, stability, and shrinking over time. These results could serve as the basis for tau isoform-specific therapeutic interventions.

## Introduction

The pathogenetic mechanisms of the tauopathies critically involve a prion-like spread of misfolded tau, often displaying disease-specific topographies and conformations[1–3]. Prion-like tau protein spread can be defined as strain-specific generation and propagation of a distinct amyloid shape within the brain[4–6]. As tau strains spread from cell to cell, the donor protein

accurately templates the misfolding of tau in the recipient cells. Capturing tau for templating requires the prion-like donor tau to select a tau conformer from the large native energy landscape that will lead to the replication of misfolded tau with specific atomic level structures corresponding to the clinical phenotypes of the tauopathies, such as repeated concussive injuries in chronic traumatic encephalopathy (CTE), frontotemporal dementias, and Alzheimer's disease (AD)[7]. The exact structural and dynamic molecular details of how tau transitions into specific amyloid forms under different clinical circumstances and cellular environments, and the resulting consequences, are still not well understood. The process starts with an intrinsically disordered tau population in a stable equilibrium of monomers (72 ± 2%), dimers (21.2 ± 0.8%), and trimers (6.6 ± 0.4%)[8], each distributed across a vast and rugged landscape of conformationally shallow and deep energy wells. Within this conformational landscape of probability states, tau can adopt folds that promote self-association by stabilizing intermolecular and intramolecular contacts, leading to oligomerization[9], fibrillization, and seeding in recipient cells[10].

Two highly studied six amino acid peptides—VQIINK in repeat domain 2 (R2) and VQIVYK in repeat domain 3 (R3)—can assemble *in vitro* into β-sheet-rich fibrils, but these fibrils are not seed-competent[11–13]. Characteristics of these sequences known as PHF6* and PHF6, respectively, have been studied by the clearance capacity of peptide mimetics targeting these amyloidogenic motifs[14–16], nanobodies targeting PHF6[17] and by enhancing the function of the chaperones Hsp40, Hsp70, and Hsp90, known to bind around PHF6[18]. While these short sequences in tau are recognized as amyloidogenic *in vitro*, little is known about the additional molecular features that confer the property of seeding. Attempts to define a minimal seed include tau trimers[19], individual repeat peptides[20], a seed-competent monomer[21], and peptides that extend the amyloidogenic hexapeptides[11,12,22]. These include a 31-amino-acid peptide (residues 306-336)[23] and a 17-amino-acid peptide (residues 295-311)[22].

Central to this pathogenic process is an interaction of a seed with a local sequence segment of endogenous, native tau, which induces conformational changes that reshape the energy landscape of the full-length protein over a large extent of its sequence. Experimental methods suggest that the unmasking of an otherwise shielded amyloidogenic sequence contributes to seeding[22]. These sites of vulnerability, when exposed, are present at several locations within the tau sequence, including the hexapeptides PHF6* and PHF6[24–26]. For instance, heparin, a cofactor that induces tau fibril nucleation and growth, expands and exposes the distance between S238C-G272C, which flanks VQIINK (PHF6*), from an average of 2.16 nm to 4.35 nm in approximately 10 minutes, well before the 12-16 hour time point when aggregation plateaus[27]. The exposure of an amyloidogenic sequence results in an increase in β-sheet structure by stacking additional tau proteins with an exposed amyloidogenic region, leading to elongation until a fibril is assembled.

We report a 19-amino-acid peptide that can seed full-length tau *in vitro* and in cell culture, thereby extending its structural impact beyond the region of its sequence. Replica Exchange molecular dynamic simulations (REMD), which were confirmed experimentally, revealed a mechanism that lowered the energy barrier toward oligomerization. The peptide selectively seeded 4R tau in cell culture, inducing sarkosyl-insoluble tau aggregates and high molecular weight oligomers that robustly propagated to daughter cells across multiple passages. The aggregation of endogenous tau in cells was observed to form β-sheet structures

with properties similar to Alzheimer brain tau oligomers. A lipid signal in proximity to the aggregate emerged as a distinct cellular feature of the aggregate.

## Results

### *A Small Tau Peptide Induces Tau Fibrils*

Two 19-amino-acid tau peptides (295-313) designated jR2R3 and jR2R3 P301L, that differ only by the presence of the P301L mutation in jR2R3 P301L (Figure 1A), can readily form fibrils[22]. jR2R3 and jR2R3 P301L span the splice junction between the second and third repeat and contain the PHF6 aggregation motif (VQIVYK)[11,14,17]. PHF6 appears in various contexts within the recently solved full-length tau fibril structures, always adopting β-strand conformations[28–31]. For tauopathies containing exclusively 4R tau (corticobasal degeneration (CBD), argyrophilic grain disease (AGD), aging-related tau astrogliopathy (ARTAG), progressive supranuclear palsy (PSP), globular glial tauopathy (GGT), GGT-PSP tauopathy (GPT)), the jR2R3 sequence folds into a strand-loop-strand motif (Figure 1B)[32]. In pure 3R tauopathies, such as Picks' disease (PiD), which lack residues present in jR2R3 and jR2R3 P301L, the PHF6 amyloidogenic sequence does not reside in the context of a strand-loop-strand (Figure 1B)[33]. For tauopathies with mixed 3R/4R isoforms (AD, CTE), the N-terminal half of the jR2R3 sequence—residues 295-305—is not present in the solved Cryo-EM structures[28,29] (Figure 1B), but NMR structures show that 3R and 4R tau are well mixed in AD-tau seeded fibrils, and the mixed fibrils reveal no structural differences in the rigid β-sheet core or the mobile domains[34]. These structural data are important for understanding the prion-like properties of the jR2R3 peptides.

jR2R3 P301L demonstrated the capacity to fibrilize under a wide range of conditions (Figure 1C, 1D). In contrast, jR2R3 could only aggregate in the presence of heparin and shaking, and even under these conditions, only some of the reactions resulted in productive fibril formation, which took more than 24 hours (Figure S1A, S1B). The aggregation of jR2R3 P301L, with and without heparin, was rapid, reaching plateaus in less than three hours. These aggregates displayed fibril-like morphologies with characteristic periodicity as observed by TEM (Figure 1C).

Next, we tested whether jR2R3 and jR2R3 P301L fibrils could seed native jR2R3 and jR2R3 P301L monomers. All jR2R3 seeds had excess heparin removed to prevent residual cofactor-induced fibrilization. In both cases, jR2R3 and jR2R3 P301L fibrils were able to propagate fibrils from jR2R3 and jR2R3 P301L monomers (Figure S1C, S1D).

We tested if jR2R3 and jR2R3 P301L fibrils could seed the larger tau constructs, Tau187-WT and Tau187-P301L (a.a. 255-441 includes core structures observed in cryo-EM tauopathies) (Figure 1A). Both peptides robustly seeded fibril growth (Figure 1C Bottom, 1D Bottom, S1E, S1F). These resulting fibrils appeared much more amorphous, but periodicity and a fibrillar appearance were readily observed. These results show that these short fragments were sufficient for propagating tau fibrils that extend well beyond the core amyloidogenic sequence which directly interacts with the peptide.

### *Seeding and Aggregation of jR2R3 P301L Induced Tau Aggregates in Cells*

We evaluated seeding in H4 cells stably expressing mClover3-Tau187-P301L, a construct that encompasses the core of all disease tau fibrils solved by Cryo-EM[28–31,33]. jR2R3

P301L fibrils seeded tau aggregates (Figure 2B Top). At concentrations of 2 μM jR2R3 P301L fibrils, 30 ± 7% of cells exhibited at least one visible tau aggregate eight hours post jR2R3 P301L seeding. The experiments described next were conducted relative to this benchmark: a seeding assay displaying the most cells with puncta (Figure 2A). Full-length mClover3-Tau constructs were evaluated for their aggregation tendencies in the presence of jR2R3 P301L fibrils. Both mClover3-0N4R-P301L, and mClover3-2N4R-P301L robustly formed aggregates when seeded by jR2R3 P301L (Figure 2B, S2A, S2B Bottom). mClover3-Tau187-WT and mClover3-0N4R-WT showed significantly less aggregation than their corresponding P301L variants (Figure 2B). Additionally, mClover3-2N4R-WT showed less aggregation than the Tau-187 constructs, potentially due to the aggregation inhibitory role of the N-terminus[35] (Figure 2B, S2B Top). More aggregates were observed in cells with mClover3-P301L constructs than the corresponding WT lines for all constructs tested, and Tau187 lines showed more aggregates when compared to full-length tau (Figure 2B Bottom, S2A, S2B). The less well-fibrillized jR2R3 peptides were unable to seed tau aggregation across a range of concentrations up to 5 μM fibril tested within the first 24 hours after seeding. Neither monomeric jR2R3 and jR2R3 P301L could seed aggregates in cells at any tested concentration or time scale.

Fluorescence recovery after photobleaching (FRAP) experiments indicated that the inclusions did not undergo fluorescence recovery after bleaching. Nine separate mClover3-Tau187-P301L jR2R3 P301L seeded aggregates were completely bleached, and no recovery of fluorescence was observed over several minutes (Figure S3A). Moreover, when large aggregates were half-bleached, there was no redistribution of fluorescence from the unbleached half of the aggregate (Figure S3B). Collectively, these results indicate that tau aggregates did not display liquid-like exchange properties with the surrounding cellular space.

***Extraction and Passaging of Cell Culture Seeded Material***

Large quantities of cells expressing mClover3-Tau187-P301L were seeded with jR2R3 P301L fibrils, from which we extracted sarkosyl soluble and insoluble material. Western blots of the soluble material revealed multiple bands labeled with MC1 at ~240 kDa which would correspond to ~6-mers of mClover3-Tau187. We then compared these patterns to those from sarkosyl soluble and insoluble fractions of tau extracted from Alzheimer brain samples. MC1 positive oligomer bands ran at molecular weights that approximated 6-mers of full-length tau (Figure 2C). Additionally, a fraction of the insoluble material ran at extremely high molecular weights that did not enter the wells. TEM images of the insoluble material extracted from seeded cells exhibited distinct fibril-like structures (Figure 2D Left). Next, the insoluble material from the cell culture lines was added back to cells expressing mClover3-Tau187-P301L to test its seeding efficacy. The fibril fractions robustly seeded tau aggregation (Figure 2D Right).

Encouraged by the strain propagation observed with cell-extracted seeding, we cultured jR2R3 P301L seeded cells for extended periods to look for the propagation of aggregates in dividing cells. Cell lines harboring aggregates induced by jR2R3 P301L were passaged at low densities, and their division was monitored. Cells with aggregates underwent cell division, and the resulting daughter cells continued to have aggregates, suggesting authentic propagation of a strain (Figure 2E). By passaging single cells into wells, we could clonally isolate cell lines that propagated the strain specifically over multiple passages.

***Demonstrating 4R Selectivity of jR2R3 P301L Seeding in Cell Culture***

If jR2R3 P301L is functioning as a prion-like moiety, we should be able to detect precise templating and propagation of a strain. In 4R tauopathies, 4R is selectively incorporated into fibrils[36,37] and the fibril structure corresponds to the specific 4R tauopathy, which spreads with high structural fidelity. Considering the complementarity of the jR2R3 and jR2R3 P301L sequences with 4R tau but not 3R tau, we hypothesized that jR2R3 P301L should be able to elongate only 4R tau isoforms. To examine selective 4R aggregate formation, we created three cell lines expressing equimolar ratios of 3R and 4R isoforms of Tau187. The two tau constructs, each labeled with a distinct fluorophore (mRuby3 or mClover3), were separated by the self-cleavable P2A sequence. This allowed for visualization isoform-selective incorporation into aggregates (Figure 2F).

As anticipated, when jR2R3 P301L fibrils were introduced into cells expressing two 4R isoforms of Tau187, aggregates a were observed in both channels (Figure 2G Left Bottom). In contrast, cells expressing two copies of the 3R isoform of Tau187 showed no formation of aggregates (Figure 2G Left Top). Finally, cells expressing one copy each of 4R and 3R Tau187 only displayed aggregates in the channel corresponding to 4R Tau187 (Figure 2G Left Middle). The cell derived material (sarkosyl extraction from jR2R3 P301L seeding) was then added to dual expressing 3R/4R Tau187 cell lines (Figure 2G Middle). The same selective seeding of 4R tau, as seen with jR2R3 P301L, was again observed. This outcome demonstrated the 4R selectivity of seeding. In comparison, seeding with AD brain-derived material, induced the formation of aggregates that exhibited fluorescence in both channels in each cell line, consistent with the mixed 3R and 4R tau isoform composition of AD brain fibrils (Figure 2G Right)[37].

***Defining the Energy Barrier to 4R Tau Fibrilization***

The observation that jR2R3 P301L could seed Tau187(4R) over Tau187(3R) led us to search for unique features of the R2-R3 junction found in 4R isoforms compared to the R1-R3 junction found in 3R isoforms. Another 19 amino acid peptide that spans the R1-R3 junction is referred to as jR1R3 (Figure 3A). Notably, jR2R3 and jR1R3 differ by only four amino acids while the amyloidogenic PHF6 region is shared in both sequences. We synthesized a peptide corresponding to the jR1R3 sequence and observed that, in contrast to the jR2R3 and jR2R3 P301L peptides, jR1R3 could neither fibrilize on its own, nor in the presence of heparin. None of the conditions tested, including rapid agitation, induced aggregation over any of the timescales tested (data not shown) despite having the amyloidogenic PHF6 sequence. We next added jR2R3 or jR2R3 P301L fibrils to jR1R3 monomers to seed jR1R3 aggregation. Again, no aggregation was observed under any condition (data not shown). Thus, the four amino acid differences between these two peptides conferred strong resistance to fibrillization.

We turned to replica exchange molecular dynamics simulations (REMD), a widely used method that enhances conformational sampling of proteins by overcoming otherwise inescapable energy barriers and thus exploring extensive free energy landscapes. How might jR1R3 avoid aggregation? A clustering analysis of the replica exchange simulations of jR2R3, jR2R3 P301L, and jR1R3 identified Cluster 1 and Cluster 2 as containing the most prevalent conformations (Figure 3B). In our molecular dynamics simulations, we've observed two distinct types of backbone H-bonds in both Cluster 1 and Cluster 2 that help stabilize a β-hairpin conformation, specifically with the GGG motif at the turn. For ease of discussion, we've termed the H-bond nearer the GGG turn motif as the "pinch". This "pinch" appears to keep the hairpin structure closely bound. On the other hand, the H-bond situated closer to the ends of the molecule, which prevents them from unraveling, is termed the "clamp". Cluster 1 has an H-bond

pinch between V/Q300 and S/K305 and an H-bond clamp between K298 and Q307; Cluster 2 has a H-bond pinch between V/Q300 and Q307 and a H-bond clamp between K298 and V309. These H-bonds appear to maintain the hairpin shape in a manner that occludes the amyloidogenic PHF6 sequence. We quantified the hairpin unfolding free energy landscapes from the replica exchange simulations of jR2R3, jR2R3 P301L, and jR1R3 as a function of the two pairs of diagnostic α-carbon distances (Figure 3C). The most populated conformation (Cluster 1) is in the bottom left of the landscape. The landscape features distinct minima at short distances indicative of stable conformations. Interestingly, jR1R3 has a significantly larger free energy barrier to unfold than jR2R3 or jR2R3 P301L, and jR1R3 lacks a clear pathway to escape the intramolecularly H-bonded Cluster 1 and Cluster 2. The higher escape energy of jR1R3 may prevent its oligomerization by protecting the amyloidogenic PHF6 sequence. This observation is consistent with the requirement for filaments to form, intramolecular backbone H-bonds must be replaced with intermolecular backbone H-bonds as occurs in the disease state (Figure 3D, see orange dashes).

The greater tendency of jR2R3, jR2R3 P301L compared to jR1R3 to form intermolecular H-bond formation, was demonstrated by REMD simulations of dimers. jR1R3 formed significantly fewer intermolecular H-bonds compared to jR2R3 and jR2R3 P301L (Figure 3E). Specifically, conformations with five or more intermolecular H-bonds are rare when either of the monomers exhibits the H-bond pattern of Cluster 1 or Cluster 2. Based on this observation, we further hypothesize that the intramolecularly H-bonded structures of jR2R3 and jR2R3 P301L in Cluster 1 and Cluster 2 confer resistance to aggregation.

These simulations suggested that an extensive H-bond network can safeguard 3R tau containing the junction sequence jR1R3 from aggregation in 4R tauopathies. While similar H-bonds might exist in the jR2R3 region, these are far less stable and have lower energy barriers, facilitating transitions to fibril competent conformations. We performed the *in silico* mutation series of each of the four amino acid differences that converted jR1R3 to jR2R3 in a stepwise manner. Simulating these fragments with explicit-water REMD to observe differences in H-bonding, electrostatic interactions, and hydrophobic interactions revealed that each successive mutation of jR1R3 weakened the protective H-bonding network, as measured by the populations of Cluster 1 and Cluster 2 (Figure 3F). All four residue differences between jR1R3 and jR2R3 modulated intramolecular hydrogen bonding which protects PHF6 from aggregation in jR1R3 and deprotects in jR2R3. Thus, the gradual weakening of the H-bonds made the peptide more prone to forming intermolecular H-bonds and ultimately aggregation.

The next experiment reversed the direction by mutagenizing jR2R3 to more closely resemble jR1R3 (Fig 3A). Remarkably, in this case, a single mutation in jR2R3 to jR2R3 S305K (a K in jR1R3 occurs in this position rather than an S) drastically increased the free energy barrier to monomer unfolding (Figure 3C Bottom Right), increased intramolecular H-bonding, and would be predicted to prevent tau aggregation. By simulating the fragments jR2R3 and jR2R3 S305K with REMD, we observed that the S305K mutation approximately doubled the population of the aggregation-resistant Cluster 1 (Figure 3F). K305's hydrophilic side chain amine tends to orient outward to the solvent (Supplementary Figure 4A), which orients its backbone carbonyl inward where it can form an H-bond with residue 300. We simulated a deprotonated lysine and saw that the doubling of the Cluster 1 population was undone Figure 3F), thus supporting our hypothesis that the charge facilitates the correct orientation of the K305 H-bond.

### *Experiments Validate of 4R Energy Barrier Simulations*

To validate these computations, a series of 3R tau constructs, with the four sequential mutations within the 1R-3R junction to match those found in the 2R-3R junction of Tau187-P301L, were introduced (Figure 3A Right). These constructs were labeled mClover-Tau187(3R)-P270L to indicate the corresponding site in the 1R-3R sequence with the Tau187-P301L mutation in the second repeat. The mutations were mClover-Tau187(3R)-P270L-E264D, mClover-Tau187(3R)-P270L-E264D-L266I, mClover-Tau187(3R)-P270L-E264D-L266I-Q269V, and mClover-Tau187(3R)-P270L-E264D-L266I-Q269V-K274S. We introduced jR2R3 P301L fibrils to cell lines stably expressing each construct and aggregates were only observed in the construct with all four mutations. (Figure 3G). This outcome validates our simulations and suggests that the local structure around the exposed PHF6 motif plays a crucial role in seeding. The aggregation observed exclusively in the 3R tau construct with all four mutations in the presence of jR2R3 P301L fibrils implies that these specific mutations could be pivotal for enabling seeding by exposure of the PHF6 sequence.

While these 4R mutations altered the resistance of 3R tau so that it became competent to undergo jR2R3 P301L 4R specific tau aggregation, the next question was whether we could prevent 4R aggregation by introducing a mutation into the second repeat that made its structure more similar to 3R tau, and hence resistant to the induction of jR2R3 P301L-induced tau aggregation. In position 305, immediately amino to the VQVII amyloidogenic sequence, a serine is present in the R2-R3 junction, and a lysine is present in R1-R3 junction. Remarkably, when jR2R3 P301L was introduced to a cell line expressing Tau187-P301L-S305K, no significant aggregation was seen (Figure 3G Bottom Right) consistent with the predictions from the REMD simulations. As expected, Tau187(3R) or Tau187(3R)-P270L mutant could not be seeded by jR2R3 P301L fibrils in any of our cell culture experiments.

### *Binding of Z70 Nanobody Inhibits Peptide-induced Seeding*

We used the previously described camelid heavy-chain-only antibody VHH Z70[17], with a binding sequence that is co-extensive with the PHF6 sequence. VHH Z70 forms five intermolecular hydrogen bonds between VHH Z70 and PHF6. The PHF6 sequence, derived from the structure of disease fibrils, aligns with the crystallized Z70 bound to a free PHF6 peptide (Figure 4A and 4B)[28]. Cell lines stably expressing mClover3-Tau187-P301L were transiently transfected with VHH Z70-mCherry and subsequently exposed to jR2R3 P301L fibrils. Twelve hours later, cells were imaged. Analysis in both the mClover-Tau187-P301L and mCherry-VHH Z70 nanobody channels revealed that cells expressing the camelid nanobody contained significantly fewer aggregates, compared to cells lacking mCherry-VHH Z70 (11 ± 7% vs 34 ± 10% of cells, $p = 2.3 \times 10^{-8}$, Figure 4C, 4D). These results suggest that VHH Z70 can inhibit jR2R3 P301L-seeded aggregation of Tau187-P301L, similar to the seeding experiment using microtubule binding region tau peptide fibrils in HEK293T biosensor lines[17].

We next pre-formed cellular aggregates by exposing cells to jR2R3 P301L fibrils first and subsequently transfected cells with mCherry-VHH Z70 in an attempt to clear established aggregates. Under these conditions there was considerable cell death and therefore it was not possible to determine whether aggregates were cleared. However, there were sufficient cells to clearly observe colocalization of the nanobody signal with aggregates (Figure 4E) and demonstrated that the nanobody recognized aggregated tau.

### *jR2R3 P301L-Seeding Induces Global Structural Modifications*

The seeded material was analyzed by dynamic electron-electron resonance (DEER) experiments to probe the atomic level structure of tau within the fibrillar aggregates. In DEER, two probes are attached at specific residues on a protein, and the experiment measures the range of distances between these probes, reflecting the conformations sampled by the protein. The results are presented as a set of probabilistic distances that correspond to the location of specific spin labels. We probed site pairs that were predicted to inform us about the tertiary fold adopted by the seeded tau constructs. The structures formed from jR2R3 P301L fiber-seeded Tau187(4R) material differed substantially from heparin-seeded fibrils (Figure 5A, 5B). Specifically, pairwise distribution plots showed broad distributions for heparin fibrils for both the 334-360 distance (Figure S4A) and the 351-373 distance (Figure 5A). This indicates a sampling of many conformations of fibrils as predicted from the Cryo-EM structures of heparin-seeded tau[31]. However, for jR2R3 P301L-seeded Tau187 fibrils, peaks were sharper, indicating a smaller sampled space compared to heparin-seeded fibrils. Interestingly, the 351-373 distance pair, which is predicted to sample widely different distances in PSP and CBD fibrils, demonstrated a substantial compaction of the P(R) curve centered at 2.5 nm (Figure 5C, 5D, 5E). This corresponds to the distance between these two residues in the PSP cryo-EM structure[28]. Compared to both the Tau187 monomer and heparin-induced Tau187 fiber measurements, this peak is both sharper and samples notably less of the P(R) space. Triplicate measurements confirm this observation. Unlike the PSP structure, the 334-360 probe pair yielded multiple distance peaks that did not correspond closely to either PSP or the CBD distances (Figure S4A, S4B, S4C, S4D). Instead, they revealed a heterogeneous distance probability distribution that is likely indicative of greater disorder across this distance. The peaks sampled differed from the heparin-induced distance pair and are narrower and distinct from monomer data. Taken together, these data suggest that the jR2R3 P301L peptide is capable of templating discrete large structural changes throughout the tau protein.

### *jR2R3 P301L-Seeded Aggregates have Cross β-strand Structure and an Associated Lipid Signal by Optical Photothermal Infrared Microscopy*

Optical photothermal infrared (O-PTIR) microscopy, which provides sub-micrometer resolution infra-red imaging[38–41] was used to probe the structure of jR2R3 P301L-seeded cellular aggregates. In O-PTIR, each pixel of the microscopic image contains an IR spectrum over a defined range of wavenumbers allowing for the investigation of the chemical and structural composition at specific fluorescent structures (Figure 6A, 6B). Measurements of the cellular aggregates revealed a significantly higher cross β-strand content compared to the cytoplasm, as indicated by the substantial difference in the mean values of the ratio of peaks at 1634 $cm^{-1}$ and 1654 $cm^{-1}$ ($p = 1.6 \times 10^{-5}$, Figure 6D). This result is consistent with the expected properties of aggregates forming fibril-like structures. Interestingly, a local increase in signal at 1750 $cm^{-1}$ associated with the aggregate was observed, indicative of a lipid signal. When compared to the cytoplasm, the difference in the ratios of 1750 $cm^{-1}$ and 1654 $cm^{-1}$ was also highly significant ($p = 7.8 \times 10^{-7}$, Figure 6D).

### *Cellular Effects of Seeded Tau Aggregates*

To examine the possibility that tau aggregates were associated with lysosomes or autophagosomes, cells were stained with either a Lamp1 or a LC3 antibody. Small, punctate signals typical of lysosomes or autophagosome did not substantially co-localized with the aggregate signals (Figure 6C). The Manders' coefficient for tau to Lamp1 overlap was 0.12 ± 0.1, and for Lamp1 overlap to tau was 0.055 ± 0.05 (N=15 cells), indicating minimal overlap. For

tau to LC3, the overlap was 0.41 ± 0.2, and LC3 to tau overlap was 0.44 ± 0.1 (N=8 cells), suggesting modest colocalization. Interestingly, a substantial overlap was observed between LC3 and the largest tau aggregates, with a Manders' coefficient of 0.90 ± 0.2 for tau overlap to LC3 under specific thresholds that capture only the largest tau aggregates (Figure 6E). Thus, there is some attraction of LC3 to the larger aggregates.

The large perinuclear aggregates of tau protein observed in our jR2R3 P301L-seeded cells hinted at the involvement of cellular degradation mechanisms beyond the capacity of traditional autophagy or proteasomal pathways to clear proteins[42], and thereby necessitate the deployment of alternative clearance strategies such as aggresomes[43,44]. To examine this possibility, we stained cells expressing aggregate induced by jR2R3 P301L with antibodies targeting SQSTM1 (also known as P62) and VCP (also known as P97). Both of these proteins have been implicated in previous studies as colocalizing with tau inclusions, suggesting a potential role in the degradation of tau aggregates[45–52]. Immunofluorescence analysis (Figure 6F, 6G) revealed that both SQSTM1 and VCP exhibited pronounced colocalization with the large tau aggregates in the jR2R3 P301L-seeded cells. This observation aligns with existing literature that demonstrates the colocalization of SQSTM1 and VCP with tau inclusions[48–53], suggesting their involvement in the degradation of tau aggregates.

***Dynamics and Heterogeneity of Tau Aggregates***

Before the introduction of seeds, all cell lines—including WT and P301L mutants—displayed typical microtubule staining patterns (Figure 2A Left, S2B, S2C). In cells with mature aggregates, which can range in size from very large (up to 20 μm) to minute, diffraction-limited specks (<250 nm), the population of tau bound to microtubules was greatly diminished (Figure 2C). Aggregates larger than 1 μm in size displayed a diverse range of morphologies, with some appearing elongated and others lumped together. This irregularity is reflected in a variable mean circularity value centered at 0.55 ± 0.25. The population of cells with the most aggregates were entirely devoid of tau microtubule staining (Figure 2E) and by four days in culture such cells dominated. In this experiment, cells actively expressing new monomeric tau preferentially partitions into aggregates rather than binding to existing microtubules suggesting that the aggregate has a greater affinity for tau than the microtubules. However, after staining with an anti-α-tubulin antibody, an intact microtubule network remained presumably associated with other microtubule-associated proteins (Figure 7A).

To systematically investigate the temporal evolution of tau aggregation, live cells were monitored for a period of 10 hours, with images of tau aggregates captured at 30-minute intervals. Aggregates did not appear to fuse but sometimes clumped together. Fragmentation of the aggregates was not observed. A few aggregates were spherical, but most were irregular in appearance. A few had a linear appearance that resembled the seeded aggregates previously observed in proximity to microtubules[54]. Individual cells were tracked, allowing for the quantification of the total area occupied by aggregates, the average size of aggregates, and the number of aggregates per cell. To enhance data reliability, we excluded cells undergoing division or exhibiting signs of cell death.

Our analysis revealed that both the total area occupied by aggregates per cell and the number of aggregates per cell followed a bi-exponential distribution (Figure 7B). We then classified changes in total aggregate area within individual cells and found that the total aggregate area decreased in 48 cells, remained stable in 267 cells, and increased in 86 cells

over the 10 hour time period (Figure 7C). We applied K-means clustering analysis to the trajectories of individual cell total area, effectively segregating the data into three distinct subpopulations based on aggregate dynamics (Figure 7D). We plotted these subpopulations and observed clear patterns of decline, stability, and growth in aggregate areas for the respective clusters (Figure 7E).

## Discussion

PHF6 and PHF6* oligomers, rich in beta-strand content[11], can form self-complementary beta-sheet pairs known as steric zippers[55], but they are unable to template tau misfolding in cells. Their inability to seed naïve tau into aggregates suggests an additional sequence is required for transcellular spread of misfolded tau in a prion-like manner. Inroads to this problem have emerged with the introduction of longer peptides that extend the 6-mer amyloidogenic core to include portions of the tau repeat 2 and 3 sequences[16,20,56,57]. This report defines a 19 amino acid peptide designated jR2R3 P301L that spans the 2R-3R junction and is capable of forming fibrillar structures. When introduced into cells this peptide can template misfolding by energetically transmitting conformational change throughout the entire tau protein in the recipient cells. In so doing, tau forms sarkosyl soluble oligomers with properties that parallel human brain tauopathies, including MC1 antibody staining, fibril-like morphologies seen by TEM, and molecular weights that approximate endogenous oligomers. Importantly, based on the design of the peptide that includes sequence uniquely present in 4R tau, it is specific for inducing pure 4R tau aggregates as occurs in AGD, PSP, CBD, ARTAG, GGT and GPT, but is unable to induce pure 3R aggregates as occurs in PiD[60–62]. The specific induction and passaging of these aggregates confirms a prion-like mechanism of tau spread capable of precise templating the donor structure. The peptide corresponds to a relatively “cleavage poor” region of tau[58] possibly related to the two histidines which is the only amino acid with a pKa within the physiological range and will make the peptide uniquely suited to be protonated inside the acidic lysosome. While mainly of interest as a heuristic probe, the resistance of the peptide to proteolysis under physiologic conditions may generate a similar peptide *in vivo*. Recently, time-resolved electron cryo-microscopy was used to detect a similar peptide described as the first intermediate amyloid considered on pathway to Alzheimer and CTE oligomers[59].

The most salient feature of prion-like templating by jR2R3 P301L is its specificity for 4R tau. The structural basis for this specificity is the strength with which a hairpin containing the amyloidogenic PHF6 region (VQIVYK) is accessible as determined by the conformational effects of the flanking sequence. By substituting specific amino acids in the flanking sequence that will weaken or strengthen access to the PHF6 region, 4R tau can become competent or incompetent to initiate a 4R tauopathy. These substitutions are derived from those amino acids in jR1R3 that depart from jR2R3 and inferred from the REMD. The simulations showed clear energetically accessible pathways from a shielded loop region due to H-bonding to a more accessible internal loop structure in jR2R3 that is prone to intermolecular H-bonds and hence oligomerization. The most remarkable observation was the single amino acid substitution, S305K, that can prevent jR2R3-induced aggregation suggesting a site where a single codon substitution could prevent 4R tauopathies. As a point of background information, S305 is the last codon of MAPT exon 10, and is included in the RNA hairpin loop that regulates exon 10 alternative splicing. Although mutations have been identified in this codon that increase 4R tau like all other splice site mutations[60] none of mutations correspond to S305K used here for its effects on the tau protein.

Three factors potentially explain why the S305K mutation inhibits 4R tau aggregation: steric hindrance of the known 4R tau folds, increased hydration at the dewetting interface during elongation, and altered intramolecular H-bonding within monomers. Among four solved 4R tau folds, three—CBD, PSP, and GGT—have an S305 oriented inwardly within the strand-loop-strand motif (Figure S5). A bulky, inwardly-pointing K305 side chain would sterically disrupt the side chain zipper, preventing these structures from forming. In contrast, a fourth 4R tau fold, termed “GPT”, presents an S305 that faces outward from the strand-loop-strand motif, leaving this motif undisturbed by the bulky K305. However, even in this context, a K305 side chain would sterically disrupt contacts with I354 and L357 potentially impeding fibrillization. Beside steric considerations, the K305 mutation might disrupt aggregation due to its positively charged side chain which interacts favorably with water. Consequently, this side chain and the adjacent residues will be more resistant to dewetting, which is an essential step in nucleation and elongation.

The exposure of intramolecular electrostatic interactions that permit the formation of hydrophobic bonds through forced association with an aqueous solvent may account for the presence of lipids we observe in association with tau aggregates. Solvent-exposed hydrophobic regions can favor interactions with low-molecular-weight hydrophobic or amphiphilic lipids known to interact with tau and induce aggregation[61]. Within intrinsically disordered proteins, lipid-binding occurs in more structured regions, such as the relatively more ordered repeat region in tau where its prion properties reside[62]. Indeed, using solid-state NMR and transmission electron microscopy, a tau construct encoding the microtubule-binding repeats and a proline-rich domain was reconstituted into cholesterol-containing phospholipid membranes in a transition from a random coil to a β-sheet conformation over weeks[63]. Cellular aggregates displayed colocalization with VCP and SQSTM1, proteins essential for aggresome formation and selective autophagy[47–49,53,64]. SQSTM1, known to interact with tau and autophagosomes, has diminished expression in Alzheimer’s disease[43] and its depletion leads to hyperphosphorylated tau accumulation[50]. Meanwhile, VCP aids in the degradation of tau aggregates[49] and is crucial for proper aggresome formation[65], implicating a critical role for both proteins in the pathogenesis of tauopathies.

These studies suggest several entry points for 4R tauopathy interventions involving either nanobodies or small molecules, but all pointing to the structure of the R2R3 spanning hairpin and relative exposure of the PHF6 amyloidogenic sequence. Structural studies suggest a similar rationale might be applied to the amyloid-beta-peptide[66]. The observation suggests that aggregates are dynamically changing their size may offer a rationale for disaggregation approaches.

### *Limitations of the Study*

Although H4 neuroglioma cells lines are an improvement over HEK293T cells used in related biosensor studies, these cells are cancerous glial cells, might not faithfully represent the responses of primary neurons, which are predominantly involved in tauopathies. The short peptides used in this study are revealing of a biophysical structure capable of revealing prion-like processes, but they have not been identified in vivo. However, short tau fragments are known to exist in the disease state and cleavage poor properties of this fragment suggest it may exist *in vivo*. To detect aggregates, we had to use lipofectamine for the delivery of tau fibrils.

While this approach has proved effective, it deviates from physiological conditions where tau fibrils would not have such assistance for cellular uptake. We did observe signals in cells exposed to jR2R3 P301L fibrils without the use of lipofectamine, but the incidence of cells containing aggregates was lower and took longer to manifest.

In consideration of these limitations, the results of this study provide valuable insights, but with the understanding that the cell model and delivery mechanisms employed might not fully recapitulate the complexities of *in vivo* systems. This research serves as a steppingstone and underscores the importance of further investigations using models that more closely mimic the physiological environment, such as iPSC-derived neurons.

**Acknowledgments**

We acknowledge support by the NIH grant 5R01AG056058-07. The authors acknowledge support from the Center for Scientific Computing at the California Nanosystems Institute (CNSI, NSF grant CNS-1725797) for the availability of high performance computing resources and support. This work used the Extreme Science and Engineering Discovery Environment, which is supported by the National Science Foundation grant ACI-1548562 (MCA05S027). J.E.S acknowledges support from the NSF (MCB-1716956). We acknowledge the use of the NRI-MCDB Microscopy Facility and the Resonant Scanning Confocal supported by NSF MRI grant DBI-1625770.

**Author Contributions**

Conceptualization, A.P.L, K.S.K, S.H., J.E.S., and S.S.; methodology, A.P.L., K.S.K., S.H., A.D., S.L., V.V., Y.B., E.K.R., J.S.J., and A.N.; investigation, A.P.L. A.D., S.L., V.V., Y.B., E.K.R., J.S.J., A.N., D.C.C., M.U., O.S., and V.F.; writing – original draft, A.P.L. and K.S.K.; writing – review and editing, A.P.L, K.S.K., A.D., S.L., V.V., Y.B., E.K.R., J.S.J., I.L., L.B., and M.V.; visualization, A.P.L. and S.L.; resources, I.S., L.B., K.S.K., and S.H.; formal analysis, A.P.L, K.S.K., S.H., S.L., V.V., A.N., and Y.B.; supervision, K.S.K., S.H., S.S., and J.E.S.; funding acquisition K.S.K., S.H., S.S., and J.E.S.

**Declaration of Interests**

K.S.K. consults for ADRx and Expansion Therapeutics and is a member of the Tau Consortium BOD.

**Main Figure Titles and Legends**

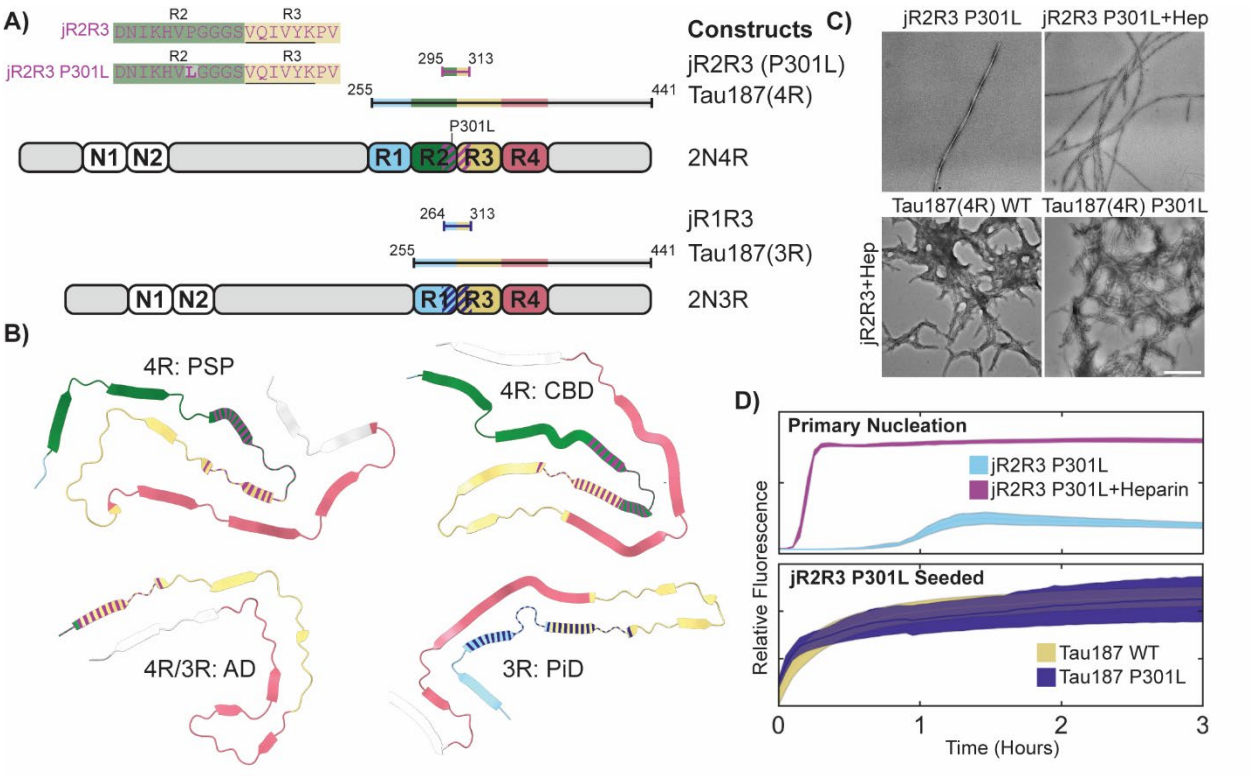


**Figure 1: Tau Constructs, Structural Representations, and Fibrilization Characteristics of jR2R3 and jR2R3 P301L** A) Overview of the tau constructs utilized in the study, including 3R and 4R isoforms. These strand loop strand sequences, designated jR2R3 and jR2R3 P301L, are shown in the top left with the PHF6 sequence underlined and residues mutated relative to jR2R3 shown in bold. The diagram also illustrates the most commonly used constructs, categorizing jR2R3, jR2R3 P301L, and Tau187(4R) as 4R tau constructs, and categorizing Tau187(3R) and jR1R3 as 3R tau constructs. The elements are color-coded for clarity with R1 highlighted in Cyan, R2 in Green, R3 in Sand, R4 in Rose, and jR2R3 and jR2R3 P301L in Purple. Dashed line on 2N4R and 2N3R represent the jR2R3/jR2R3 P301L junctions. B) PDB structures representing 4R tauopathies (PSP with PDB ID: 7P65[32] and CBD with PDB ID: 6VHA[67], mixed 4R/3R tauopathy (AD with PDB ID: 6VHL[67]), and 3R tauopathy (PiD with PDB ID: 6GX5[33]). The jR2R3 and jR2R3 P301L constructs are centrally located in 4R tauopathies and are hypothesized to be minimal elements capable of specifically templating 4R isoforms. In mixed 4R/3R and 3R tauopathies, jR2R3 and jR2R3 P301L are absent due to splicing of the R2 repeat, which would hinder templating by jR2R3 and jR2R3 P301L due to clashes with the R1 alternatively spliced sequences in 3R sequences. The structures are colored with the conventions established in (A), with jR2R3 and jR2R3 P301L represented by striped coloration over their respective sequences. C) TEM images displaying the fibrilization of jR2R3 P301L in the absence (Top Left) and presence of heparin (Top Right), as well as seeding of jR2R3 P301L with heparin seeds. Scale Bar: 500 µm. D) (Top) ThT assays comparing jR2R3 P301L fibrilization alone (cyan) and with heparin (purple). (Bottom) ThT assays after adding jR2R3 P301L heparin-seeded fibrils to Tau187 WT (sand) and Tau187 P301L (indigo) monomers. Error bounds represent standard error of the mean.

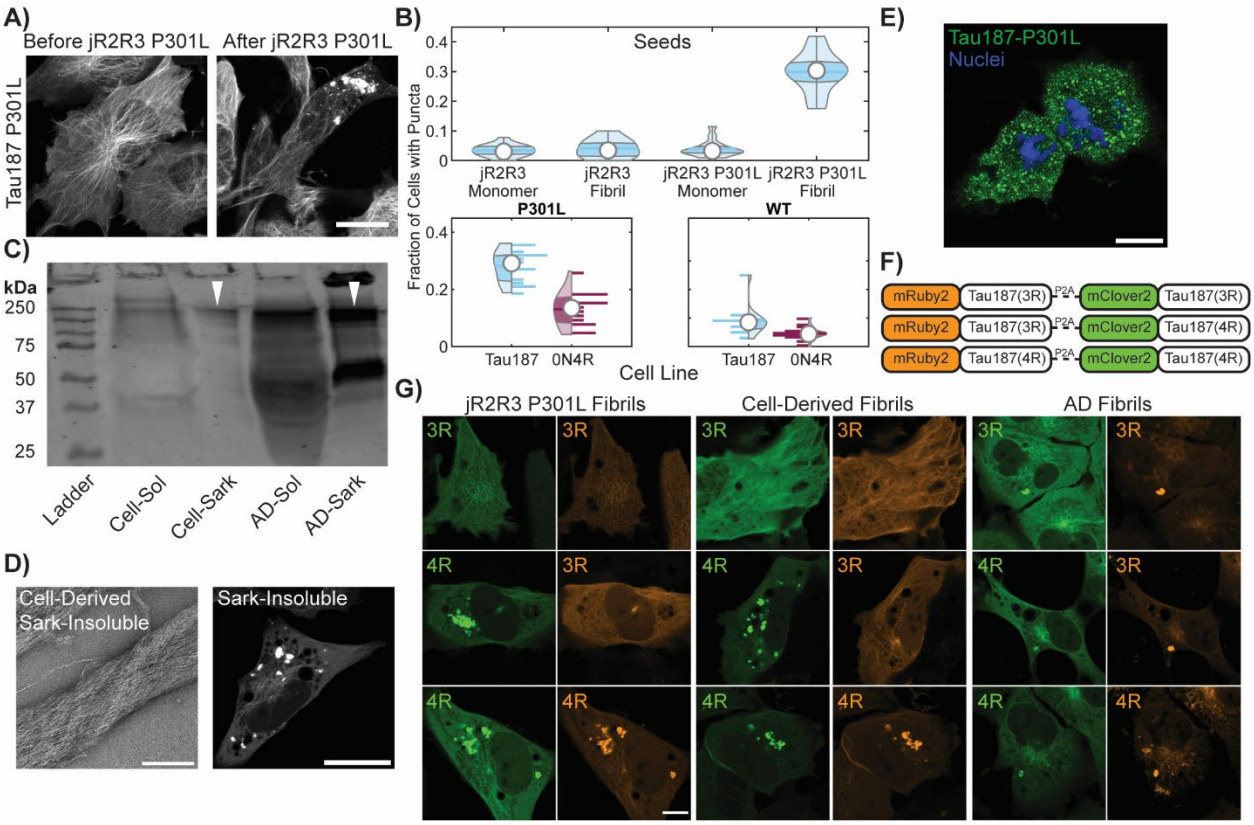


**Figure 2: Tau Aggregation Formation, Propagation, and their Characteristics in Cells Seeded with jR2R3 P301L Fibrils** A) H4 cell stably expressing mClover3-Tau187-P301L, seeded with jR2R3 P301L fibrils, imaged at 0- and 12-hours post jR2R3 P301L fibril addition. Scale bar: 20 µm. B) Violin plots of mClover2-Tau187-P301L cell lines seeded with the peptide series of monomers and fibrils (Top). Further analysis focused on jR2R3 P301L fibrils added to cells lines expressing Tau187 P301L or full length 0N4R P301L (Bottom Left) or Tau187 WT and full length 0N4R WT (Bottom right). Percentage of cells with puncta were 5 ± 2.3% of 0N4R WT cells had puncta and 13 ± 6 % of 0N4R P301L cells had puncta. Tau187 lines had the most puncta with Tau187 WT having 9 ± 5.5 % and Tau187 P301L having 28 ± 5 %. C) Western blot of sarkosyl soluble and insoluble material from mClover3-Tau187-P301L cells seeded with jR2R3 P301L and material derived from AD brain samples. Blot stained with the disease-specific conformational tau antibody (MC1). Similar-sized oligomers observed for both cell-derived and patient-derived material highlighted with white triangles. D) (Left) TEM of sarkosyl insoluble material derived from cell lines. Scale bar: 250 nm. (Right) Sarkosyl insoluble fractions were added to the original mClover3-Tau187-P301L cell lines showing seeding of puncta after 12 hours. Scale bar: 20 µm. E) Cells seeded with jR2R3 P301L undergo division and propagate aggregates to daughter cells. Green: Tau187-P301L, Blue: Hoescht. Scale bar: 20 µm. F) Schematic of the three constructs used for testing the selective templating of either the 4R or 3R isoform of tau by jR2R3 P301L. Each construct consists of either the 4R or 3R isoform of tau fused to mRuby3, and is expressed concurrently with another 4R or 3R isoform of tau fused to mClover3. A P2A cleavage site between the two tau fusions ensures equimolar expression of the two fusions from the same expression cassette. G) 12 hours after the addition of jR2R3 P301L, cells expressing two copies of 4R tau showed aggregates in both channels (Left Bottom), cells expressing both 4R and 3R isoforms showed aggregates exclusively in the 4R channel (Left Middle), whereas cells expressing two copies of 3R tau exhibited no aggregates

(Left Top). This provides strong evidence that isoform-specific templated elongation is the primary mode of propagation in these cell lines. As a control, fibrils from AD samples, which are characteristic of a mixed 4R/3R tauopathy, seeded both 3R and 4R isoforms as anticipated (Middle). Additionally, cell-derived material was reintroduced to the described cell-lines, and selective 4R seeding was again observed (Right). Scale bar: 20 µm.

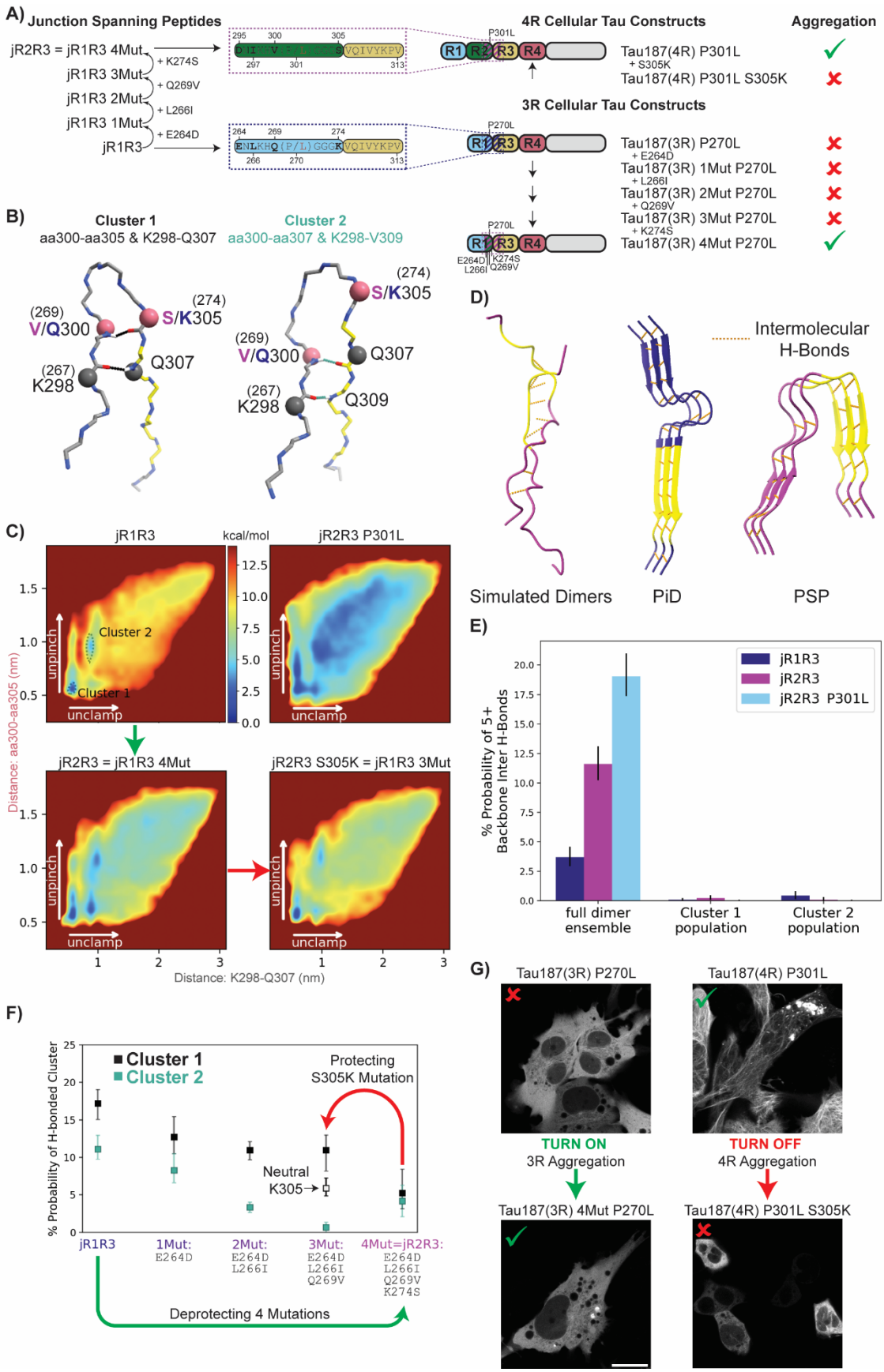
A)
Junction Spanning Peptides
jR2R3 = jR1R3 4Mut
+ K274S
jR1R3 3Mut
+ Q269V
jR1R3 2Mut
+ L266I
jR1R3 1Mut
+ E264D
jR1R3
4R Cellular Tau Constructs
Aggregation
Tau187(4R) P301L
+ S305K
Tau187(4R) P301L S305K
3R Cellular Tau Constructs
Tau187(3R) P270L
+ E264D
Tau187(3R) 1Mut P270L
+ L266I
Tau187(3R) 2Mut P270L
+ Q269V
Tau187(3R) 3Mut P270L
+ K274S
Tau187(3R) 4Mut P270L
B)
Cluster 1
aa300-aa305 & K298-Q307
Cluster 2
aa300-aa307 & K298-V309
C)
jR1R3
kcal/mol
jR2R3 P301L
Cluster 2
Cluster 1
unpinch
unclamp
jR2R3 = jR1R3 4Mut
jR2R3 S305K = jR1R3 3Mut
Distance: aa300-aa305 (nm)
Distance: K298-Q307 (nm)
D)
Intermolecular H-Bonds
Simulated Dimers
PiD
PSP
E)
jR1R3
jR2R3
jR2R3 P301L
% Probability of 5+ Backbone Inter H-Bonds
full dimer ensemble
Cluster 1 population
Cluster 2 population
F)
Cluster 1
Cluster 2
Protecting S305K Mutation
Neutral K305
% Probability of H-bonded Cluster
jR1R3
1Mut: E264D
2Mut: E264D L266I
3Mut: E264D L266I Q269V
4Mut=jR2R3: E264D L266I Q269V K274S
Deprotecting 4 Mutations
G)
Tau187(3R) P270L
Tau187(4R) P301L
TURN ON
3R Aggregation
TURN OFF
4R Aggregation
Tau187(3R) 4Mut P270L
Tau187(4R) P301L S305K

**Figure**

**3: Comparative Analysis of Energy Landscapes and Hydrogen Bonding in jR2R3, jR2R3 P301L, and jR1R3 Monomers and Dimers** A) Schematics illustrating the relationships between the junction spanning peptides used in the simulations and the Tau187 constructs used in the cellular seeding assays. On the left, junction spanning peptides representing the residues 295(264)-313 in the 2N4R numbering scheme are shown. These regions are highlighted with dotted boxes in the Tau187 constructs used in the study. For each Tau187 construct, a red x or a green check mark annotates if jR2R3 P301L was able to induce puncta in the respective cell line. For 3R constructs the P270L mutation corresponds to the P301L mutation seen in 4R isoforms. B) Illustration of two most populated clusters from REMD simulations. Cluster 1 (Top, Black) highlights hydrogen bonds between aa300-aa305 and K298-Q307. Cluster 2 (Bottom, Cyan) highlights hydrogen bonds between aa300-aa307 and K298-V309. For residues with different numbering in 3R and 4R isoforms, the alternate numbering is shown in parenthesis. Rose colored balls and black colored balls represent the 4 residues that are used to construct the energy landscapes in (C). C) Energy landscapes of α-carbon distances K298-Q307 and aa300-aa305 for jR1R3 (Top Left), jR2R3 P301L (Top Right), jR2R3 (jR2R3 = jR1R3 4Mut) (Bottom Left), and jR1R3 3Mut (Bottom Right). The y-axis represents the distance between aa300-aa305, while the x-axis represents the distance between K298-Q307 and are colored as in (B). Clusters 1 and 2 from (B) are annotated in the top left panel as dotted lines. Mutations that transition the jR1R3 peptide to the jR2R3 peptide diminish the energy wells stabilizing the hydrogen bonding in Clusters 1 and 2 (Green arrow), while mutation S305K in the jR2R3 construct reestablishes the barriers and turns off aggregation (Red arrow). D) Representative conformations of dimer, with intermolecular hydrogen bonds depicted as yellow dots. A dimer conformation with both monomers in open states and featuring nine intermolecular backbone hydrogen bonds is shown on the left, compared to the structures from PiD (middle) and PSP (Right). E) Analysis of dimer simulations for jR2R3, jR2R3 P301L, and jR1R3, showing differences in intermolecular hydrogen bonding. jR1R3 exhibits reduced intermolecular hydrogen bonding compared to jR2R3 and jR2R3 P301L. Bars represent 90% confidence intervals. Oligomers with high hydrogen bonding (i.e., 5 or more intermolecular backbone hydrogen bonds) are rarely formed when one monomer is in a closed conformation. F) Monitoring the formation of two pairs of hydrogen bonds as jR2R3 transitions into jR1R3 through sequential amino acid swaps. Cluster 1 is represented by black boxes and Cluster 2 is represented with cyan boxes. Cluster 1 with a neutral K305 is shown as an unfilled black box. The bars represent 67% confidence intervals. Protecting (Red) and deprotecting (Green) mutations are highlighted as arrows and represent the mutations shown in panels (C) and (G). G) jR2R3 P301L added to cell lines expressing Tau187(3R) P270L did not form aggregates (Top Left), but when added to cells expressing Tau187(3R) 4mut P270L formed aggregates (Bottom Left). jR2R3 P301L added to cell lines expressing Tau187(4R) P301L formed aggregates (Top Right), but when added to cells expressing Tau187(4R) S305K P301L no aggregates were observed (Bottom Right).

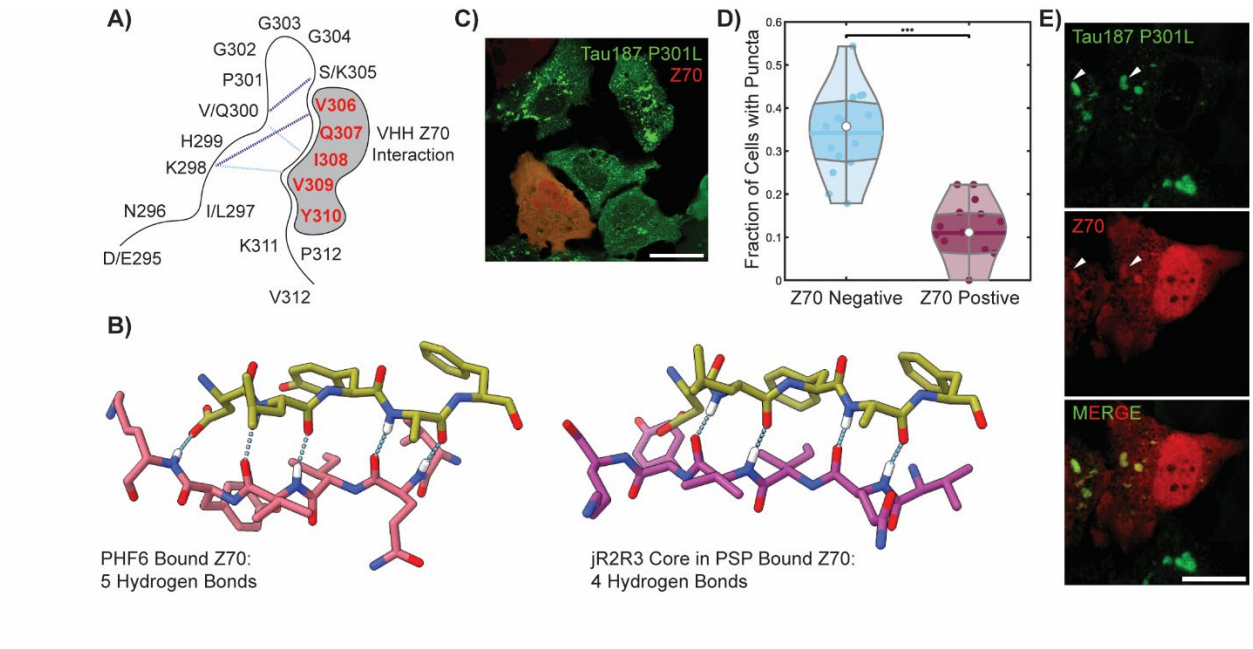


**Figure 4: Investigation the Effect of VHH Z70 Nanobody on jR2R3 P301L-Induced Tau Fibrilization in Cells** A) Schematic representation of the SLS hairpin and its most populated hydrogen bonds as determined with molecular dynamics (Cluster 1 in purple and Cluster 2 in cyan dashed lines). The interaction with ZHH Z70 is highlighted by gray shading and its interaction site, the PHF6 motif is represented in red. B) The crystal structure (PDB:7QCQ[17]) of VHH Z70 in olive bound to PHF6 in rose reveals five hydrogen-bond contacts between the molecules (Left). An alignment of the PHF6 sequence from the PSP fibril (PDB:7P65[32], purple, Right) with that bound in the crystal structure of VHH Z70 shows an RMSD 0.848, with four potential hydrogen bond contacts, suggesting that the VHH Z70 nanobody could recognize 4R tauopathy fibrils. C) jR2R3 P301L sonicated fibrils were introduced to stable H4 cell lines expressing mClover3-Tau187-P301L, with a subset of cells transiently expressing a nanobody-mCherry fusion against PHF6 (VHH Z70) in red. Notably, cells expressing VHH Z70 generated fibrils less frequently than those that did not express VHH Z70. Scale bar: 30 µm. D) Quantification of the data from (C) indicates that cells with VHH Z70 formed puncta 11 ± 7% of the time, whereas those without VHH Z70 exhibited puncta in 34 ± 10% of cells, suggesting an inhibitory effect of VHH Z70 on fibril formation. E) Upon addition to preformed aggregates, the VHH Z70 nanobody exhibited clear colocalization with a subset of the tau aggregates, as indicated by white arrow heads. Scale bar: 20 µm.

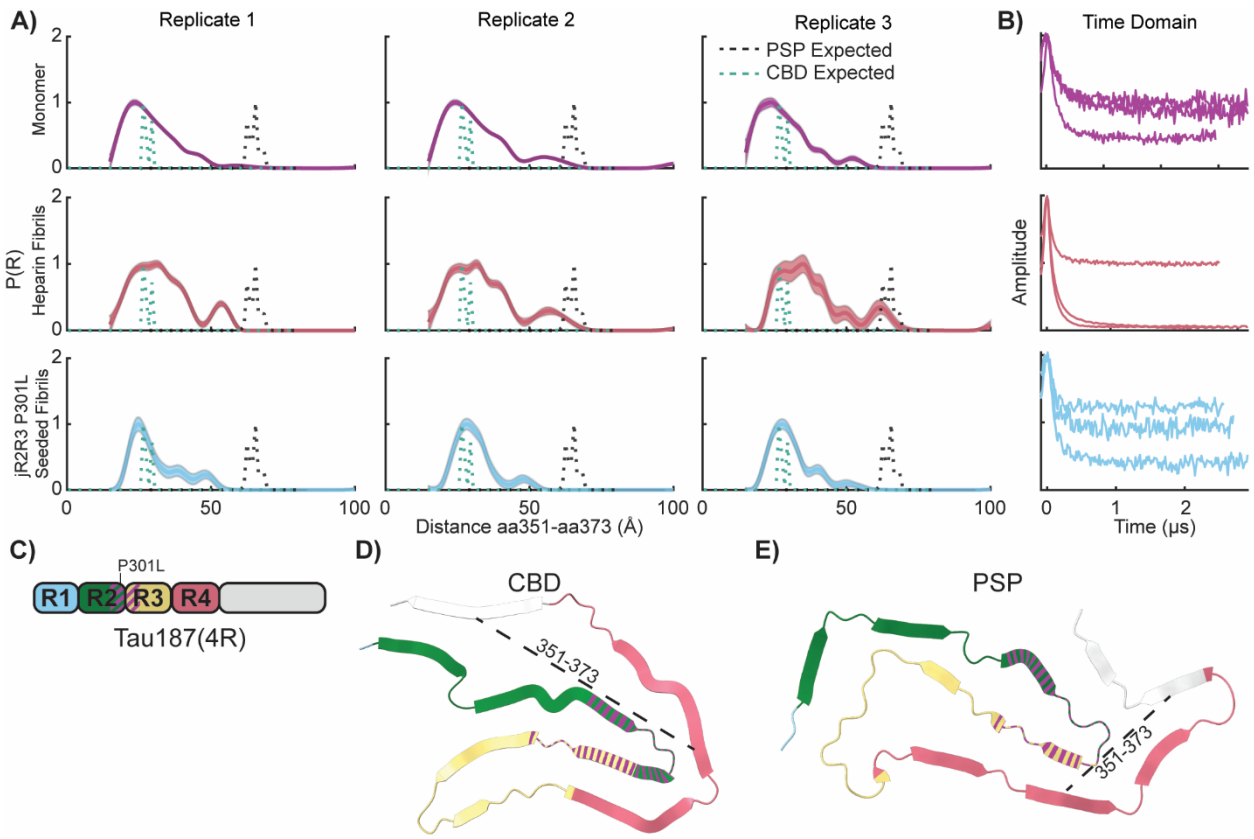


**Figure 5: Comparative Analysis of DEER Measurements for Monomeric and Fibrillar Tau Configurations** A) DEER distance distribution plots (P(R)) for the 351-373 spin-pair distances in various tau configurations. The monomer is represented in purple, jR2R3 P301L seeded fibril in cyan, heparin fibril in rose, while the predicted distances for CBD are in black and PSP are in teal. Triplicates of each condition are plotted across the columns. B) The time domain data for each of the replicates plotted in (A). C) Schematic of the coloring used to represent Tau187(4R) as described in Figure 1A. D) Hypothetical representation of distances expected if a pure CBD fold was sampled. E) Hypothetical representation of distances expected if a pure PSP fold was sampled. The figure provides insight into the conformational distinctions between tau monomers, jR2R3 P301L-seeded fibrils, and pathological tau configurations.

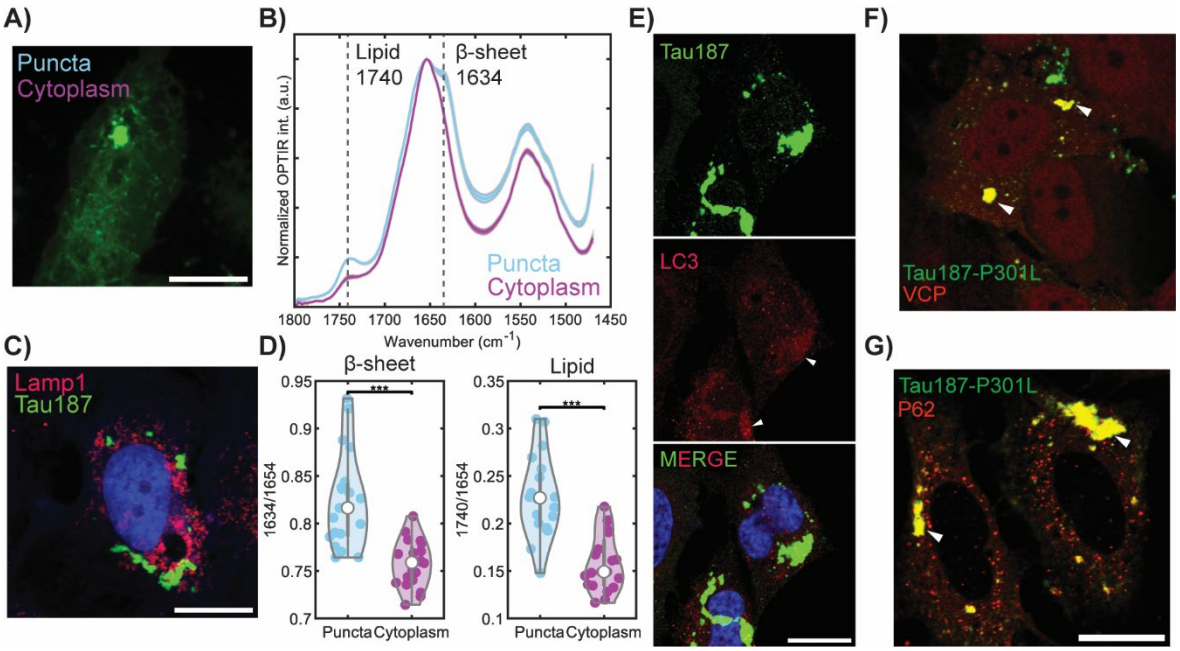


**Figure 6: Presence of Lipid in jR2R3 P301L-Seeded Cellular Aggregates using Optical Photothermal Infrared Microscopy and Analysis of Autophagosome and Lysosomal Markers** A) O-PTIR interrogation of cells expressing mClover3-Tau187-P301L. Measurements (depicted as cyan and purple dots) were taken on tau aggregates and cytoplasm, respectively. Scale bar: 15 µm. B) Averaged spectra of measurements from (A), with distinct peaks at 1740 $cm^{-1}$ (lipid) and 1634 $cm^{-1}$ (β-sheet) in aggregates. Error bars represent SEM. C) Representative cell stained with Lamp1 antibody (red) to visualize lysosomes. Tau187 puncta signal (green) shows minimal colocalize with Lamp1 signal. Scale bar: 20 µm. D) Quantification of lipid and β–sheet content from 20 independent measurements in aggregates (cyan) and cytoplasm (purple), for both lipid and B-sheet in aggregates revealing highly significant differences. E) Tau (green) co-localization with LC3 (red) indicates significant overlap with the largest tau aggregates (white arrows), suggesting a possible early stage of autophagy recruitment. Scale bar: 20 µm. E, F) Colocalization of protein degradation markers VCP (red, E) and P62 (red, F) with large tau aggregates (green). Scale bar: 20 µm.

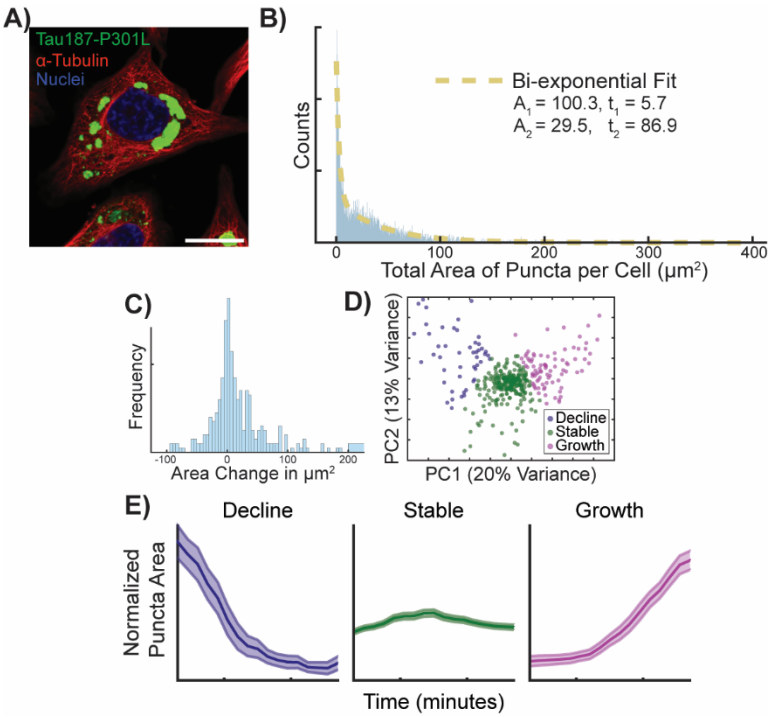


**Figure 7: Growth, Stability, and Shrinkage in Puncta** A) Microscopy images showing intact microtubule network (α-tubulin staining in red) despite no visible tau binding to microtubules after large aggregates form (green). Scale bar: 20 μm. B) Histogram of the total puncta area per cell fit to a bi-exponential decay curve (sand dotted line). C) Monitoring cells with jR2R3 P301L-induced aggregates for 10 hours, imaging every 30 minutes. The total change in aggregate area per cell was plotted as a histogram. D) PCA analysis on the trajectories of the changing aggregate area; K-means clustering identified three clusters that represent cells with declining (indigo), stable (green), and growing (purple) aggregate areas. E) The average of the individual trajectories based on K-means clustering are plotted, showing decline, stability, or growth. Shaded area represents the SEM of the normalized, combined trajectories. E) Colocalization of protein degradation markers VCP and P62 (red) with large tau aggregates (green). Scale bar: 20 μm.

## STAR Methods

### Resource Availability

#### *Lead Contact*

Further information and requests for resources and reagents should be directed to and will be fulfilled by Kenneth Kosik (kosik@lifesci.ucsb.edu).

#### *Materials Availability*

Materials included in this manuscript will be shared upon request.

#### *Data and Code Availability*

All raw data is available upon request. Code is deposited on https://github.com/samlobe/tau-seeding-2023/.

**Experimental model and study participant details**

Human cell lines used in this manuscript are summarized in the key resources table.

**Method Details**

***Cloning of Tau Constructs***

We assembled mClover3-2N4R-WT constructs using the HiFi Reaction Kit from NEB. Additionally, we generated various isoforms such as mClover3-0N3R-WT, mClover3-0N4R-WT along with truncations including mClover3-Tau187(4R)-WT, mClover3-Tau187(3R)-WT through deletion PCRs and KLD reactions using NEB kits.

Using site-directed mutagenesis, we created mutant constructs, specifically mClover3-Tau187-P301L, mClover3-0N4R-P301L, and mClover3-2N4R-P301L. Additionally, using similar techniques, we created mClover3-Tau187(3R)-P270L, mClover3-Tau187(3R)-P270L-E264D, mClover3-Tau187(3R)-P270L-E264D-L266I, mClover3-Tau187(3R)-P270L-E264D-L266I-V269Q, and mClover3-Tau187(3R)-P270L-E264D-L266I-V269Q-S274K

Constructs with dual tau expression, such as mRuby3-Tau187-P301L-P2A-mClover3-Tau187-P301L, mRuby3-Tau187(3R)-P2A-mClover3-Tau187-P301L, and mRuby3-Tau187(3R)-P2A-mClover3-Tau187(3R), were synthesized using HiFi reactions with the previously mentioned constructs as templates.

We procured pET28a-Tau187-WT-His and pEt28a-Tau187-P301L-His constructs from Genescript and constructed pET28a-Tau187(3R) using deletion PCR.

For DEER experiments, we generated Tau187 Cysless constructs with one or two cysteine mutations using site-directed mutagenesis.

***Preparation of Purified Tau Constructs***

Peptides obtained from Genescript, all featuring uncapped termini, were dissolved in dd$H_2O$ and stored immediately as 100 μM aliquots at -80˚C. The aggregation process was facilitated in a 50 mL Eppendorf tube where the stock peptide was reduced to a 50 μM concentration using 20 mM HEPES, pH 7.4, accompanied by a 4:1 ratio addition of 200 μM heparin (average molecular weight 16 kDa). Continuous shaking at 200 rpm in a 37°C incubator was performed for 24 hours. The resultant fibrils were isolated using a 50 kDa cuttoff concentrator and rinsed 3 times with MilliQ water to remove excess peptide and monomeric peptide. The fibrils were then lyophilized overnight using a FreeZone 2.5 Liter -84C Benchtop Freeze Dryer. Upon quantification of the fibril mass, we reconstituted the seed stock to 1 mM using 20 mM HEPES, pH 7.4, and froze it at −80°C.

Tau187 expression and purification procedures followed previously reported methods[68]. We transformed E. coli BL21 (DE3) cells with various plasmids and stored the cells as frozen glycerol stocks at −80°C. An overnight growth of cells in 10 mL Luria Broth preceded the inoculation of 1 L of fresh LB. The incubated the cells at 37°C at 200 rpm, supplementing with 10 μg/mL kanamycin, until an optical density at λ = 600nm of 0.6–0.8 was achieved. We

induced expression by introducing 1 mM isopropyl-ß-D-thiogalactoside for 2–3 h. Post expression, cells were harvested via centrifugation at 4500 g for 20 min.

Harvested cells were resuspended in lysis buffer (Tris-HCl, pH = 7.4, 100 mM NaCl, 0.5 mM DTT, 0.1 mM EDTA) supplemented with 1 Pierce protease inhibitor tablet per 5 mL lysis buffer, 1 mM PMSF, 2 mg/mL lysozyme, 20 µg/mL DNase and 10 mM MgCl2, and incubated on ice for 30 min. The samples underwent three freeze-thaw cycles using liquid nitrogen, followed by 10-minute centrifugation at 10,000 rpm to discard cell debris. Another, 1 mM PMSF was added, and samples were then heated at 65°C for 12 minutes and cooled on ice for 20 minutes before undergoing another round of centrifugation to remove the precipitant.

The clear supernatant was incubated with pre-equilibrated Ni-NTA resins overnight in buffer A (20 mM sodium phosphate, pH = 7.0, 500 mM NaCl, 10 mM imidazole, 100 µM EDTA). We subsequently transferred the resins to a column and washed with 20 mL of buffer A, 25 mL buffer B (20 mM sodium phosphate, pH = 7.0, 1 M NaCl, 20 mM imidazole, 0.5 mM DTT, 100 µM EDTA). We collected the purified protein through elution with 15 mL of buffer C (20 mM sodium phosphate, pH = 7.0, 0.5 mM DTT, 100 mM NaCl, 300 mM imidazole). SDS-PAGE confirmed the purity of the fractions. After buffer exchange into a DTT-free working buffer (20 mM ammonium acetate, pH 7.0), we immediately froze the proteins and stored them at −80°C.

### *Thioflavin T Experiments*

Thioflavin (ThT) experiments were conducted using a BioTek Synergy 2 fluorescent plate reader. Each well of a 384-well plate (Corning, low volume non-binding surface, black with clear flat bottom) contained 50 µM of SLS or Tay monomer, 20 µM ThT, 12.5 µM heparin or 12% seed 20 mM HEPES HEPES buffer (pH 7.4), making a total volume of 20 µL per well.

The plate reader was set to a temperature of 37°C and allowed time to equilibrate. Subsequently, ThT fluorescence intensity was recorded at excitation and emission wavelengths of 440 nm and 485 nm, respectively. Measurements were taken every 2 minutes until a plateau in fluorescence intensity was observed. Each experiment was performed with five replicates and repeated three times using independent samples, typically spanning a total time of 48 hours.

### *TEM Analysis*

For transmission electron microscopy (TEM) analysis, 5 µL of recombinant tau fibril samples were placed onto a glow-discharged copper grid (Electron Microscopy Science, FCF-200-Cu) for 20 seconds before blotting dry with filter paper. The samples were then stained by applying 5 µL of 1.5% (w/v) uranyl acetate solution, immediately blotting dry. An additional 5 µL of uranyl acetate solution was added for 60 seconds, followed by blotting dry. The samples were examined using a Thermo Scientific Talos G2 200X TEM/STEM microscope operating at 200 kV and room temperature. The grids were imaged using a Ceta II CMOS 4k x 4k camera at the specified magnifications.

### *Object Segmentation and Tracking*

All image processing was carried out using Python 3.10.12. The time series of cell images featuring puncta were loaded utilizing the OpenCV-python 4.7.0.72 package. The analysis of these images was conducted using scikit-image 0.19.3 package.

Initially, nuclei were identified by applying Li thresholding[69] to the Hoechst intensity image Objects with size smaller than 100 $\mu m^2$ were excluded from further analysis as noise, and the remaining connected regions were labeled as separate nuclei.

Subsequently, the mClover3-Tau187 fluorescence intensity images, after being subjected to blurring, were used for the detection of cell bodies through mean thresholding[70]. The masks for nuclei and cell bodies were combined to form complete cell masks. The watershed algorithm was employed, using labeled nuclei as seeds, to delineate individual cells.

Cells obtained through this process were tracked across successive frames using centroid tracking. In this approach, a centroid in a new frame was associated with the nearest centroid in the preceding frame, marking them as the same object.

Puncta were detected using the Laplacian of Gaussian blob detection method. In each frame, puncta located within the mask of a cell object were assigned to that cell.

### ***Computational Modeling***

*REMD Simulations*

Replica-exchange molecular dynamics (REMD) simulations were carried out using the Gromacs package (versions 2019.6 and 2020.1) [71,72]. Simulations were conducted in rhombic dodecahedral boxes of approximately 7.5 nm length, comprising 19-mer peptide(s), around 7860 TIP4P-D water molecules, and neutralizing chlorine ions. Peptides were simulated with zwitterionic termini. In the case of monomer simulations, the peptides began in extended conformations. For dimer simulations, the peptides were initialized in the two most common monomer conformations based on a Daura clustering analysis with a 4Å RMSD cutoff, and they were separated by a couple of nanometers.

The force field AMBER99SB-disp[73] was used, and periodic boundary conditions were applied along all three box vectors. The simulations included an initial 5 ns run in the NPT ensemble at 1 bar pressure and 300 K. The v-rescale thermostat (0.5 ps time constant for temperature coupling) and the Parrinello-Rahman barostat (3 ps time constant for pressure coupling) were used for this step. Next, 5 ns long NVT simulations with the Nose-Hoover thermostat (3 ps time constant for temperature coupling) were performed at 300 K temperature using the average box-size from the final three ns of the previous NPT step[74,75]. Throughout the simulations, the Particle Mesh Ewald (PME) method was used for calculating the electrostatic interactions with a grid-spacing of 0.12 nm[76]. A time step of 2.5 fs was employed using a leap-frog integrator[77]. A cutoff distance of 1.2 nm was set for all nonbonded interactions. For simulations excluding MTSL, the LINCS algorithm was used to constrain bonds with hydrogens[78]. Water molecules were maintained fully rigid using the SETTLE algorithm[79].

Subsequently, 60 replica systems were created at temperatures ranging from 300 K and 456 K: The temperatures of the replicas were: 300.0, 301.9, 303.8, 305.7, 307.7, 309.7, 311.7, 313.7, 315.8, 317.9, 320.0, 322.1, 324.3, 326.5, 328.7, 330.9, 333.2, 335.5, 337.8, 340.1, 342.5, 344.9, 347.3, 349.7, 352.2, 354.7, 357.2, 359.7, 362.3, 364.9, 367.5, 370.1, 372.8, 375.5, 378.2, 380.9, 383.7, 386.5, 389.3, 392.1, 395.0, 397.9, 400.8, 403.7, 406.7, 409.7, 412.7, 415.8, 418.9, 422.0, 425.2, 428.4, 431.6, 434.9, 438.2, 441.6, 445.0, 448.5, 452.0, 455.6 K. Each replica underwent a 5 ns NVT equilibration run per without exchanging replicas.

Following this, the replicas were subjected to 5 ns equilibration runs with replica exchanged occurring every 3 ps, achieving an average exchange probability of about 30%. This was followed by production REMD simulations ranging from, 500-750 ns per replica. The initial 40 ns were discarded for further equilibration, and certain simulations employed longer equilibration times as discussed in the next paragraph.

Equilibration times were determined using a heuristic that maximizes the number of effectively uncorrelated measurements. The autocorrelation function was integrated for equilibration times in 10 ns increments starting from 50 ns, and the equilibration time with the most effectively uncorrelated measurements was chosen. Dimer simulation equilibration times ranging from 80 to 140 ns were selected by maximizing the number of effectively uncorrelated intermolecular hydrogen bond counts. Autocorrelation functions were measured using pymbar's timeseries module. Confidence intervals were determined with bootstrapping. Residues were assigned secondary structures using the DSSP algorithm[1] in mdtraj. ChimeraX and Pymol were employed for visualizing conformations. Hydrogen bonding analysis was conducted in MDAnalysis, utilizing distance cutoffs of 3.5 Å and angle cutoffs of 140° for determining hydrogen bonds. Energy landscapes were generated by measuring the 2D probability density, taking a logarithm, scaling by Boltzmann's constant and temperature, and applying Gaussian interpolation to smooth the landscape.

*Water Triplet Angle Analysis*

The water triplet angle distribution refers to the distribution of angles formed by the oxygen of a central water and the oxygens of each pair of its neighboring water molecules. This distribution has been demonstrated to reveal patterns in the structing of water in response to different solutes and interfaces[80,81]. In this study, the distribution of hydration water was computed to be 4.25 Å around the heavy atoms of each residue's backbone or side chain. The 4.25 Å cutoff corresponds to the second minimum in the radial distribution function (RDF) between the heavy atoms of the backbone or side chain and the oxygen atoms of water. Neighboring water molecules were defined as those having oxygen atoms within 3.4 Å of the central water molecule. The hydrophilic signature was defined as the fraction of hydration waters around each peptide that form angles between 45-50° with adjacent waters, normalized by the fraction of bulk waters forming angles between 45-50° with adjacent waters. Conformations were analyzed based on data extracted every 10 ps from REMD simulations. Each frame contained statistically independent water triplet angle measurements, which were based on measured autocorrelation times. Confidence intervals of 67% were determined though bootstrapping with over 1000 independent measurements taken with replacement.

***Cell Seeding Experiments***

H4 neuroglioma cells stably expressing either mClover3-Tau187-WT, mClover3-Tau187-P301L, mClover3-0N4R-WT, mClover3-0N4R-P301L, mClover3-2N4R-WT, or mClover3-2N4R-P301L were cultured in DMEM, supplemented with 10% FBS, 100 µg/ml penicillin/streptomycin, and 500 µg/ml geneticin. The cell cultures were maintained in a humidified atmosphere of 5% $CO_2$ at 37 °C. For seeding experiments, cells were plated in 96-well plates at a density of 20,000 cells per well. On the following day, cells were transfected with various tau species (at a final concentration of 2 µM unless stated otherwise) using 1.25 µL of Lipofectamine 2000 (Thermo Fisher) per well. The tau seeds were subjected to sonication for 30 seconds using the microtip of a Qsonica sonicator, operating at a 30% duty cycle. For the quantification of the assay, cells containing one or more puncta were counted and normalized by dividing by the total number of

cells in each well. Each well in the cultured plate contributed one data point, and the quantification results were obtained from at least five independent cultures.

For experiments assessing the relative incorporation of different tau isoforms, H4 cell stably expressing mRuby3-Tau187-P301L-P2A-mClover3-Tau187-P301L, mRuby3-Tau187(3R)-P2A-mClover3-Tau187-P301L, mRuby3-Tau187(3R)-P2A-mClover3-Tau187(3R), were cultured following the aforementioned protocol.

### *Spin Labeling of Tau*

Tau187, with its native cysteines mutated to serines and the specified residues mutated to cysteines, was expressed and spin-labeled to investigate distances between two sets of target residues (residues 351 and 373, and residues 334-360). The native cysteines at 291 and 322 were mutated to serines. Additionally, a similar tau construct without any cysteines (referred to as tau-cysless) was expressed and purified. The protein was spin-labelled using MTSL ((1-Acetoxy-2,2,5,5-tetramethyl-δ-3-pyrroline-3-methyl) Methanethiosulfonate), which was purchased from Toronto Research Chemicals.

Before the labeling process, the samples were treated with a10x molar excess of DTT to reduce any cysteine residues. The DTT was subsequently removed using a PD-10 desalting column. Subsequently, a 10x molar excess of MTSL was added to the free cysteine residues and the mixture was incubated with the protein at 4˚C overnight. After the incubations, excess MTSL was removed using a PD-10 desalting column.

The labelling efficiency, which is defined as the molar ratio of attached spin labels to cysteine residues, was found to be between 50-60% for double-cysteine mutants and approximately 90% for the single-cysteine mutant.

### **Fluorescence-guided OPTIR imaging setup, spectral measurement, and data processing.**

OPTIR spectroscopy and co-registered fluorescence imaging were performed on a mIRage LS microscope (Photothermal Spectroscopy Corp.). The mid-IR laser used as the photothermal pump source was pulsing at 100 kHz repetition rate with 1% duty cycle. The visible probe source was a continuous wave laser with a center wavelength of 532 nm. The counter-propagation geometry of the mid-IR and the visible beam was used. The mid-IR beam was focused on the sample plane below the sample substrate ($CaF_2$) with a reflective objective (40x, 0.78NA, Pike Technologies), and the visible beam was focused on the sample plane from the top with a refractive objective (50x, 0.8NA, Olympus). Epi-detected light was collected and focused on a photodiode. The OPTIR signal was demodulated with a lock-in amplifier at 100 KHz. The system was enclosed and purged under gentle nitrogen flow to minimize water vapor interference of the spectra interpretation. For co-registered widefield fluorescence imaging, a filter cube set suitable for mClover3 excitation and emission was used. Typical power at the sample for mid-IR and visible were a few mW depending on the sample locations.

To prepare for OPTIR spectroscopy measurements, the cells were rinsed twice with deionized water before drying in the air. For the data acquisition, we first acquired widefield fluorescence imaging to reveal the tau distribution in cells. We then pinned to puncta regions and puncta-free regions in cells to acquire OPTIR spectra. The spectra spanned 1480 to 1800 $cm^{-1}$ (5.55 to 6.75 μm), covering protein amide II, protein amide I, and lipids signal. All raw spectra were normalized

with mid-IR power spectra to reveal the sample-related IR peaks. For the OPTIR spectra presented in the manuscript, OPTIR spectra were normalized to OPTIR intensity at 1654 $cm^{-1}$. For secondary structure quantification, β-sheet to α-helix ratio was calculated using OPTIR intensity at 1634 $cm^{-1}$ and 1654 $cm^{-1}$. Lipid contents were quantified by normalizing OPTIR intensity at 1740 $cm^{-1}$ to 1654 $cm^{-1}$. For each cell, we acquired at least 8 spectra at different puncta and puncta-free locations, where the mean intensity of the ratioed value was used to represent a single cell. Ten cells were used to perform statistical analysis.

### *Sarkosyl Extraction from Tau187 Cell Lines and AD Brains*

jR2R3 P301L fibrils were transfected in H4 cells that overexpressed the mClover3-Tau187-P301L construct, as previously described. After incubating the transfected cells overnight, the cells were washed and collected. Tau187 puncta were extracted a solution containing 2% sarkosyl in A68 buffer (10 mM Tris-HCl pH 7.5, with 10% sucrose, 0.8 M NaCl, 1mM EGTA). The A68 buffer was supplemented with PMSF and a protease inhibitor. A manual cell scraper was employed to collect the cell extracts. The samples were then sonicated for 15 seconds at 30% amplitude and incubated at 37˚ C for 30 minutes. After incubation, cell extracts were centrifuged at 113,000 g for 20 minutes at 25˚C. The sarkosyl-soluble fraction was collected and the remaining pellets were washed with 30mM Tris-HCL (pH 7.5). The samples were then centrifuged again at 113,000 g for 20 minutes at 25˚C. The sarkosyl-insoluble fractions were resuspended in 30 mM Tris-HCl (pH 7.5) and sonicated for 15 seconds at 30% amplitude.

Brain samples used in this study were sourced from the New York Brain Bank at Columbia University. The specific region of the brain from which the samples were obtained was the BA38 temporal pole, and the specimens showed neuropathologic changes associated with Alzheimer's disease. Before processing, the samples were equilibrated to -20˚C for 30 minutes, and then sliced into 0.6 micron-wide sections to accumulate a total of 0.5 grams of material. The brain tissue was homogenized in 2% sarkosyl in A68 buffer (10 mM Tris-HCl, pH 7.5, containing 10% sucrose, 0.8 M NaCl, 1 mM EGTA). At 6% (w/v) using a glass Dounce homogenizer. PMSF and protease inhibitors were added to the A68 buffer. After homogenization, the samples were centrifuged at 113,000 g for 20 minutes at 25˚C. The sarkosyl-soluble fraction was collected, and the pellets were washed with 30 mM Tris-HCl (pH 7.5). Samples were centrifuged again at 113,000 g for 20 minutes at 25˚C. The sarkosyl-insoluble fractions were resuspended in 30 mM Tris-HCl (pH 7.5) and sonicated for 15 seconds at 30% amplitude.

### *Western Blotting*

The protein concentrations of the samples were determined using a Pierce BCA Protein Assay Kit from Thermo Fisher Scientific. Standard SDS-PAGE was performed using both the sarkosyl-soluble and sarkosyl-insoluble fractions derived from cell and AD brain extractions. The samples were loadd on a 4–20% Mini-PROTEAN® TGX™ Precast Protein Gel from Bio-Rad. Precision Plus Protein Dual Color Standards ladder from Bio-Rad was used as a reference for molecular weights. For the western blot staining, the MC1 antibody hybridoma conditioned media was employed, which was kindly provided by the lab of Peter Davies. The immunoblots were imaged using a Licor Gel Imaging Station and subsequently analyzed with Fiji imaging software.

### *DEER*

To prepare the heparin fibrils for the DEER analysis, a sample mixture was created by mixing tau187(spin-labeled) and tau-cys-less at a 1:20 molar ratio (5 μM:100 μM) molar ratio and

incubating it with heparin at a 1:4 molar ratio of tau to heparin. The mixture was incubated at 37°C for 24 hours. For preparing jR2R3 P301L seeded tau fibrils, instead of heparin, 50% seeds (by molar percentage) were added to the same mixture and incubated at 37°C for 24 hours. The formation of fibrils was verified using ThT binding assay and TEM analysis. After fibrillization, the fibrils were centrifuged at 15000 rpm to pellet them, and the supernatant was discarded. The pellets were washed three to four times with $D_2O$ based 20 mM HEPES buffer to eliminate any remaining monomers. The final pellets were resuspended in 28 μL of $D_2O$ based 20 mM HEPES buffer, mixed with 12 μL D8-glycerol (making up 30% of the total volume), and transferred to a 2 mm diameter quartz tube before being flash-frozen using liquid nitrogen.

The four-pulse DEER experiments were conducted at 65 K on a Q-band Bruker E580 Elexsys pulse EPR spectrometer operating at approximately 34 GHz, and equipped with a 300 W Traveling Wave Tube (TWT) amplifier. The DEER pulse sequence used was: $p_{obs}/2 – t_1 – p_{obs} – (t-p_{pump}) – (t_2-t) – p_{obs} – t_2 – echo.$ Rectangular observe pulses were used with lengths set to $p_{obs}/2$ = 10-12 ns and $p_{obs}$ = 20-24 ns. A chirp πpump pulse was applied with a length of 20-24 ns and a frequency width of 133 MHz. The observed frequency was set 150 MHz higher than the center of the pump frequency range. $t_1$ was 180 ns and $t_2$ was varied between 1.8 ms and 2.4 ms. The DEER experiment was accumulated over ~approximately 12 hours.

The DEER data analysis was carried out using LongDistances software with Tikhonov regularization. The background signal, which arises from non-specific spin-spin interactions other than the intramolecular spin pairs and can interfere with the data, was minimized by using spin dilution with non-spin labeled tau. Additionally, singly spin-labeled tau (at site 351) was used to prepare fibrils, and the resulting signal was fit to determine the background dimensionality, which was found to be approximately 2 for the fibrils. These values were used for background subtraction for the respective fibrils. Other parameters were kept constant for all data to enable accurate comparison between samples. The background-corrected signal was transformed to a distance distribution, $P(Ree)$, by Tikhonov regularization with non-negativity constraint employing LongDistances software by Altenbach. The error in $P(Ree)$ was estimated using the bootstrapping method available in the LongDistances software.

## References


1. Lee, V.M.-Y., Goedert, M., and Trojanowski, J.Q. (2001). Neurodegenerative Tauopathies. Annu. Rev. Neurosci. *24*, 1121–1159. 10.1146/annurev.neuro.24.1.1121.

2. Goedert, M., Eisenberg, D.S., and Crowther, R.A. (2017). Propagation of Tau Aggregates and Neurodegeneration. Annu. Rev. Neurosci. *40*, 189–210. 10.1146/annurev-neuro-072116-031153.

3. Uemura, N., Uemura, M.T., Luk, K.C., Lee, V.M.-Y., and Trojanowski, J.Q. (2020). Cell-to-cell transmission of tau and α-synuclein. Trends Mol. Med. *26*, 936–952. 10.1016/j.molmed.2020.03.012.

4. Clavaguera, F., Bolmont, T., Crowther, R.A., Abramowski, D., Frank, S., Probst, A., Fraser, G., Stalder, A.K., Beibel, M., Staufenbiel, M., et al. (2009). Transmission and spreading of tauopathy in transgenic mouse brain. Nat. Cell Biol. *11*, 909–913. 10.1038/ncb1901.

5. Kaufman, S.K., Del Tredici, K., Thomas, T.L., Braak, H., and Diamond, M.I. (2018). Tau seeding activity begins in the transentorhinal/entorhinal regions and anticipates phospho-tau pathology in Alzheimer's disease and PART. Acta Neuropathol. *136*, 57–67. 10.1007/s00401-018-1855-6.

6. DeVos, S.L., Corjuc, B.T., Oakley, D.H., Nobuhara, C.K., Bannon, R.N., Chase, A., Commins, C., Gonzalez, J.A., Dooley, P.M., Frosch, M.P. (2018). Synaptic Tau Seeding Precedes Tau Pathology in Human Alzheimer's Disease Brain. Front. Neurosci. *12*, 1-15. 10.3389/fnins.2018.00267.

7. Vaquer-Alicea, J., Diamond, M.I., and Joachimiak, L.A. (2021). Tau strains shape disease. Acta Neuropathol. *142*, 57–71. 10.1007/s00401-021-02301-7.

8. Paul, S.S., Lyons, A., Kirchner, R., and Woodside, M.T. (2022). Quantifying Oligomer Populations in Real Time during Protein Aggregation Using Single-Molecule Mass Photometry. ACS Nano. 10.1021/acsnano.2c05739.

9. Bloom, G.S. (2014). Amyloid-β and Tau: The Trigger and Bullet in Alzheimer Disease Pathogenesis. JAMA Neurol. *71*, 505–508. 10.1001/jamaneurol.2013.5847.

10. Šarić, A., Michaels, T.C.T., Zaccone, A., Knowles, T.P.J., and Frenkel, D. (2016). Kinetics of spontaneous filament nucleation via oligomers: Insights from theory and simulation. J. Chem. Phys. *145*, 211926. 10.1063/1.4965040.

11. Ganguly, P., Do, T.D., Larini, L., LaPointe, N.E., Sercel, A.J., Shade, M.F., Feinstein, S.C., Bowers, M.T., and Shea, J.-E. (2015). Tau Assembly: The Dominant Role of PHF6 (VQIVYK) in Microtubule Binding Region Repeat R3. J. Phys. Chem. B *119*, 4582–4593. 10.1021/acs.jpcb.5b00175.

12. Goux, W.J., Kopplin, L., Nguyen, A.D., Leak, K., Rutkofsky, M., Shanmuganandam, V.D., Sharma, D., Inouye, H., and Kirschner, D.A. (2004). The Formation of Straight and Twisted Filaments from Short Tau Peptides. J. Biol. Chem. *279*, 26868–26875. 10.1074/jbc.M402379200.

13. Fagnen, C., Giovannini, J., Catto, M., Voisin-Chiret, A.S., and Sopkova-de Oliveira Santos, J. (2022). On the Tracks of the Aggregation Mechanism of the PHF6 Peptide from Tau Protein: Molecular Dynamics, Energy, and Interaction Network Investigations. ACS Chem. Neurosci. *13*, 2874–2887. 10.1021/acschemneuro.2c00314.

14. Seidler, P.M., Boyer, D.R., Rodriguez, J.A., Sawaya, M.R., Cascio, D., Murray, K., Gonen, T., and Eisenberg, D.S. (2018). Structure-based inhibitors of tau aggregation. Nat. Chem. *10*, 170–176. 10.1038/nchem.2889.

15. Altendorf, T., Gering, I., Santiago-Schübel, B., Aghabashlou Saisan, S., Tamgüney, G., Tusche, M., Honold, D., Schemmert, S., Hoyer, W., Mohrlüder, J., et al. (2023). Stabilization of Monomeric Tau Protein by All D-Enantiomeric Peptide Ligands as Therapeutic Strategy for Alzheimer's Disease and Other Tauopathies. Int. J. Mol. Sci. *24*, 2161. 10.3390/ijms24032161.

16. Aillaud, I., and Funke, S.A. (2023). Tau Aggregation Inhibiting Peptides as Potential Therapeutics for Alzheimer Disease. Cell Mol. Neurobiol. *43*, 951–961. 10.1007/s10571-022-01230-7.

17. Danis, C., Dupré, E., Zejneli, O., Caillierez, R., Arrial, A., Bégard, S., Mortelecque, J., Eddarkaoui, S., Loyens, A., Cantrelle, F.-X., et al. (2022). Inhibition of Tau seeding by targeting Tau nucleation core within neurons with a single domain antibody fragment. Mol. Ther. *30*, 1484–1499. 10.1016/j.ymthe.2022.01.009.

18. Mok, S.-A., Condello, C., Freilich, R., Gillies, A., Arhar, T., Oroz, J., Kadavath, H., Julien, O., Assimon, V.A., Rauch, J.N., et al. (2018). Mapping Interactions with the Chaperone Network Reveals Factors that Protect Against Tau Aggregation. Nat. Struct. Mol. Biol. *25*, 384–393. 10.1038/s41594-018-0057-1.

19. Mirbaha, H., Holmes, B.B., Sanders, D.W., Bieschke, J., and Diamond, M.I. (2015). Tau Trimers Are the Minimal Propagation Unit Spontaneously Internalized to Seed Intracellular Aggregation. J. Biol. Chem. *290*, 14893–14903. 10.1074/jbc.M115.652693.

20. Annadurai, N., Malina, L., Malohlava, J., Hajdúch, M., and Das, V. (2022). Tau R2 and R3 are essential regions for tau aggregation, seeding and propagation. Biochimie *200*, 79–86. 10.1016/j.biochi.2022.05.013.

21. Mirbaha, H., Chen, D., Mullapudi, V., Terpack, S.J., White, C.L., Joachimiak, L.A., and Diamond, M.I. (2022). Seed-competent tau monomer initiates pathology in a tauopathy mouse model. J. Biol. Chem. *298*, 102163. 10.1016/j.jbc.2022.102163.

22. Chen, D., Drombosky, K.W., Hou, Z., Sari, L., Kashmer, O.M., Ryder, B.D., Perez, V.A., Woodard, D.R., Lin, M.M., Diamond, M.I., et al. (2019). Tau local structure shields an amyloid-forming motif and controls aggregation propensity. Nat. Commun. *10*, 2493. 10.1038/s41467-019-10355-1.

23. Stöhr, J., Wu, H., Nick, M., Wu, Y., Bhate, M., Condello, C., Johnson, N., Rodgers, J., Lemmin, T., Acharya, S., et al. (2017). A 31-residue peptide induces aggregation of tau's microtubule-binding region in cells. Nat. Chem. *9*, 874–881. 10.1038/nchem.2754.

24. Barghorn, S., and Mandelkow, E. (2002). Toward a Unified Scheme for the Aggregation of Tau into Alzheimer Paired Helical Filaments. Biochemistry *41*, 14885–14896. 10.1021/bi026469j.

25. von Bergen, M., Friedhoff, P., Biernat, J., Heberle, J., Mandelkow, E.-M., and Mandelkow, E. (2000). Assembly of τ protein into Alzheimer paired helical filaments depends on a local sequence motif (306VQIVYK311) forming β structure. Proc. Natl. Acad. Sci. *97*, 5129–5134. 10.1073/pnas.97.10.5129.

26. von Bergen, M., Barghorn, S., Li, L., Marx, A., Biernat, J., Mandelkow, E.-M., and Mandelkow, E. (2001). Mutations of Tau Protein in Frontotemporal Dementia Promote Aggregation of Paired Helical Filaments by Enhancing Local β-Structure. J. Biol. Chem. *276*, 48165–48174. 10.1074/jbc.M105196200.

27. Eschmann, N.A., Georgieva, E.R., Ganguly, P., Borbat, P.P., Rappaport, M.D., Akdogan, Y., Freed, J.H., Shea, J.-E., and Han, S. (2017). Signature of an aggregation-prone conformation of tau. Sci. Rep. *7*, 1–10. 10.1038/srep44739.

28. Scheres, S.H., Zhang, W., Falcon, B., and Goedert, M. (2020). Cryo-EM structures of tau filaments. Cur. Opin. Struct. Biol. *64*, 17–25. 10.1016/j.sbi.2020.05.011.

29. Zhang, W., Tarutani, A., Newell, K.L., Murzin, A.G., Matsubara, T., Falcon, B., Vidal, R., Garringer, H.J., Shi, Y., Ikeuchi, T., et al. (2020). Novel tau filament fold in corticobasal degeneration. Nature *580*, 283–287. 10.1038/s41586-020-2043-0.

30. Fitzpatrick, A.W.P., Falcon, B., He, S., Murzin, A.G., Murshudov, G., Garringer, H.J., Crowther, R.A., Ghetti, B., Goedert, M., and Scheres, S.H.W. (2017). Cryo-EM structures of tau filaments from Alzheimer's disease. Nature *547*, 185–190. 10.1038/nature23002.

31. Zhang, W., Falcon, B., Murzin, A.G., Fan, J., Crowther, R.A., Goedert, M., and Scheres, S.H. (2019). Heparin-induced tau filaments are polymorphic and differ from those in Alzheimer's and Pick's diseases. eLife *8*, e43584. 10.7554/eLife.43584.

32. Shi, Y., Zhang, W., Yang, Y., Murzin, A.G., Falcon, B., Kotecha, A., van Beers, M., Tarutani, A., Kametani, F., Garringer, H.J., et al. (2021). Structure-based Classification of Tauopathies. Nature *598*, 359–363. 10.1038/s41586-021-03911-7.

33. Falcon, B., Zhang, W., Murzin, A.G., Murshudov, G., Garringer, H.J., Vidal, R., Crowther, R.A., Ghetti, B., Scheres, S.H.W., and Goedert, M. (2018). Structures of filaments from Pick's disease reveal a novel tau protein fold. Nature *561*, 137–140. https://doi.org/10.1038/s41586-018-0454-y.

34. Dregni, A.J., Duan, P., Xu, H., Changolkar, L., El Mammeri, N., Lee, V.M.-Y., and Hong, M. (2022). Fluent molecular mixing of Tau isoforms in Alzheimer's disease neurofibrillary tangles. Nat. Commun. *13*, 2967. 10.1038/s41467-022-30585-0.

35. Combs, B., and Kanaan, N.M. (2017). Exposure of the Amino Terminus of Tau Is a Pathological Event in Multiple Tauopathies. Am. J. Pathol. *187*, 1222–1229. 10.1016/j.ajpath.2017.01.019.

36. Arai, T., Ikeda, K., Akiyama, H., Shikamoto, Y., Tsuchiya, K., Yagishita, S., Beach, T., Rogers, J., Schwab, C., and McGeer, P.L. (2001). Distinct isoforms of tau aggregated in neurons and glial cells in brains of patients with Pick's disease, corticobasal degeneration and progressive supranuclear palsy. Acta Neuropathol. *101*, 167–173. 10.1007/s004010000283.

37. Tarutani, A., Miyata, H., Nonaka, T., Hasegawa, K., Yoshida, M., Saito, Y., Murayama, S., Robinson, A.C., Mann, D.M.A., Tomita, T., et al. (2021). Human tauopathy-derived tau strains determine the substrates recruited for templated amplification. Brain *144*, 2333–2348. 10.1093/brain/awab091.

38. Bai, Y., Yin, J., and Cheng, J.-X. (2021). Bond-selective imaging by optically sensing the mid-infrared photothermal effect. Sci. Adv. *7*, eabg1559. 10.1126/sciadv.abg1559.

39. Pavlovetc, I.M., Podshivaylov, E.A., Chatterjee, R., Hartland, G.V., Frantsuzov, P.A., and Kuno, M. (2020). Infrared photothermal heterodyne imaging: Contrast mechanism and detection limits. J. Appl. Phys. *127*, 165101. 10.1063/1.5142277.

40. Xia, Q., Yin, J., Guo, Z., and Cheng, J.-X. (2022). Mid-Infrared Photothermal Microscopy: Principle, Instrumentation, and Applications. J. Phys. Chem. B *126*, 8597–8613. 10.1021/acs.jpcb.2c05827.

41. Prater, C., Bai, Y., Konings, S.C., Martinsson, I., Swaminathan, V.S., Nordenfelt, P., Gouras, G., Borondics, F., and Klementieva, O. (2023). Fluorescently Guided Optical Photothermal Infrared Microspectroscopy for Protein-Specific Bioimaging at Subcellular Level. J. Med. Chem. *66*, 2542–2549. 10.1021/acs.jmedchem.2c01359.

42. Gorantla, N.V., and Chinnathambi, S. (2021). Autophagic Pathways to Clear the Tau Aggregates in Alzheimer's Disease. Cell Mol. Neurobiol. *41*, 1175–1181. 10.1007/s10571-020-00897-0.

43. Rahman, M.A., Rahman, M.H., Mamun-Or-Rashid, A.N.M., Hwang, H., Chung, S., Kim, B., and Rhim, H. (2022). Autophagy Modulation in Aggresome Formation: Emerging Implications and Treatments of Alzheimer's Disease. Biomedicines *10*, 1027. 10.3390/biomedicines10051027.

44. Hyttinen, J.M.T., Amadio, M., Viiri, J., Pascale, A., Salminen, A., and Kaarniranta, K. (2014). Clearance of misfolded and aggregated proteins by aggrephagy and implications for aggregation diseases. Ageing Res. Rev. *18*, 16–28. 10.1016/j.arr.2014.07.002.

45. Zatloukal, K., Stumptner, C., Fuchsbichler, A., Heid, H., Schnoelzer, M., Kenner, L., Kleinert, R., Prinz, M., Aguzzi, A., and Denk, H. (2002). p62 Is a Common Component of Cytoplasmic Inclusions in Protein Aggregation Diseases. Am. J. Pathol. *160*, 255–263. 10.1016/S0002-9440(10)64369-6.

46. Carrettiero, D.C., Almeida, M.C., Longhini, A.P., Rauch, J.N., Han, D., Zhang, X., Najafi, S., Gestwicki, J.E., and Kosik, K.S. (2022). Stress routes clients to the proteasome via a BAG2 ubiquitin-independent degradation condensate. Nat. Commun. *13*, 3074. 10.1038/s41467-022-30751-4.

47. Sánchez-Martín, P., and Komatsu, M. (2018). p62/SQSTM1 – steering the cell through health and disease. J. Cell Sci. *131*, jcs222836. 10.1242/jcs.222836.

48. Babu, J.R., Geetha, T., and Wooten, M.W. (2005). Sequestosome 1/p62 shuttles polyubiquitinated tau for proteasomal degradation. J. Neurochem. *94*, 192–203. 10.1111/j.1471-4159.2005.03181.x.

49. Saha, I., Yuste-Checa, P., Da Silva Padilha, M., Guo, Q., Körner, R., Holthusen, H., Trinkaus, V.A., Dudanova, I., Fernández-Busnadiego, R., Baumeister, W., et al. (2023). The AAA+ chaperone VCP disaggregates Tau fibrils and generates aggregate seeds in a cellular system. Nat. Commun. *14*, 560. 10.1038/s41467-023-36058-2.

50. Ramesh Babu, J., Lamar Seibenhener, M., Peng, J., Strom, A.-L., Kemppainen, R., Cox, N., Zhu, H., Wooten, M.C., Diaz-Meco, M.T., Moscat, J., et al. (2008). Genetic inactivation of p62 leads to accumulation of hyperphosphorylated tau and neurodegeneration. J. Neurochem. *106*, 107–120. 10.1111/j.1471-4159.2008.05340.x.

51. Blaudin de Thé, F.-X., Lassus, B., Schaler, A.W., Fowler, S.L., Goulbourne, C.N., Jeggo, R., Mannoury la Cour, C., Millan, M.J., and Duff, K.E. (2021). P62 accumulates through neuroanatomical circuits in response to tauopathy propagation. Acta Neuropathol. Commun. *9*, 177. 10.1186/s40478-021-01280-w.

52. Abisambra, J.F., Jinwal, U.K., Blair, L.J., O'Leary, J.C., Li, Q., Brady, S., Wang, L., Guidi, C.E., Zhang, B., Nordhues, B.A., et al. (2013). Tau Accumulation Activates the Unfolded Protein Response by Impairing Endoplasmic Reticulum-Associated Degradation. J. Neurosci. *33*, 9498–9507. 10.1523/JNEUROSCI.5397-12.2013.

53. Xu, Y., Zhang, S., and Zheng, H. (2019). The cargo receptor SQSTM1 ameliorates neurofibrillary tangle pathology and spreading through selective targeting of pathological MAPT (microtubule associated protein tau). Autophagy *15*, 583–598. 10.1080/15548627.2018.1532258.

54. Dimou, E., Katsinelos, T., Meisl, G., Tuck, B.J., Keeling, S., Smith, A.E., Hidari, E., Lam, J.Y.L., Burke, M., Lövestam, S., et al. (2023). Super-resolution imaging unveils the self-replication of tau aggregates upon seeding. Cell Rep. *42*, 112725. 10.1016/j.celrep.2023.112725.

55. Sawaya, M.R., Sambashivan, S., Nelson, R., Ivanova, M.I., Sievers, S.A., Apostol, M.I., Thompson, M.J., Balbirnie, M., Wiltzius, J.J.W., McFarlane, H.T., et al. (2007). Atomic structures of amyloid cross-β spines reveal varied steric zippers. Nature *447*, 453–457. 10.1038/nature05695.

56. Wu, L., Madhavan, S.S., Tan, C., and Xu, B. (2022). Hexameric Aggregation Nucleation Core Sequences and Diversity of Pathogenic Tau Strains. Pathogens *11*, 1559. 10.3390/pathogens11121559.

57. Larini, L., Gessel, M.M., LaPointe, N.E., Do, T.D., Bowers, M.T., Feinstein, S.C., and Shea, J.-E. (2013). Initiation of assembly of tau(273-284) and its ΔK280 mutant: an experimental and computational study. Phys. Chem. Chem. Phys. *15*, 8916–8928. 10.1039/C3CP00063J.

58. Sampognaro, P.J., Arya, S., Knudsen, G.M., Gunderson, E.L., Sandoval-Perez, A., Hodul, M., Bowles, K., Craik, C.S., Jacobson, M.P., and Kao, A.W. (2023). Mutations in α-synuclein, TDP-43 and tau prolong protein half-life through diminished degradation by lysosomal proteases. Mol. Neurodeg. *18*, 29. 10.1186/s13024-023-00621-8.

59. Lövestam, S., Li, D., Wagstaff, J.L., Kotecha, A., Kimanius, D., McLaughlin, S.H., Murzin, A.G., Freund, S.M.V., Goedert, M., Scheres, S.H.W. . Disease-specific tau filaments assemble via polymorphic intermediates. Preprint in bioRxiv. https://www.biorxiv.org/content/10.1101/2023.07.24.550295v1.

60. Iijima, M., Tabira, T., Poorkaj, P., Schellenberg, G.D., Trojanowski, J.Q., Lee, V.M.-Y., Schmidt, M.L., Takahashi, K., Nabika, T., Matsumoto, T., et al. (1999). A distinct familial presenile dementia with a novel missense mutation in the tau gene. NeuroReport *10*, 497.

61. King, M.E., Gamblin, T.C., Kuret, J., and Binder, L.I. (2000). Differential Assembly of Human Tau Isoforms in the Presence of Arachidonic Acid. J. Neurochem. *74*, 1749–1757. 10.1046/j.1471-4159.2000.0741749.x.

62. Deryusheva, E., Nemashkalova, E., Galloux, M., Richard, C.-A., Eléouët, J.-F., Kovacs, D., Van Belle, K., Tompa, P., Uversky, V., and Permyakov, S. (2019). Does Intrinsic Disorder in Proteins Favor Their Interaction with Lipids? Proteomics *19*, 1800098. 10.1002/pmic.201800098.

63. El Mammeri, N., Gampp, O., Duan, P., and Hong, M. (2023). Membrane-induced tau amyloid fibrils. Commun. Biol. *6*, 467. 10.1038/s42003-023-04847-6.

64. Ono, M., Komatsu, M., Ji, B., Takado, Y., Shimojo, M., Minamihisamatsu, T., Warabi, E., Yanagawa, T., Matsumoto, G., Aoki, I., et al. (2022). Central role for p62/SQSTM1 in the elimination of toxic tau species in a mouse model of tauopathy. Aging Cell *21*, e13615. 10.1111/acel.13615.

65. Mukkavalli, S., Klickstein, J.A., Ortiz, B., Juo, P., and Raman, M. (2021). The p97–UBXN1 complex regulates aggresome formation. J. Cell Sci. *134*, jcs254201. 10.1242/jcs.254201.

66. Khaled, M., Rönnbäck, I., Ilag, L.L., Gräslund, A., Strodel, B., and Österlund, N. (2023). A Hairpin Motif in the Amyloid-β Peptide Is Important for Formation of Disease-Related Oligomers. J. Am. Chem. Soc. 10.1021/jacs.3c03980.

67. Arakhamia, T., Lee, C.E., Carlomagno, Y., Duong, D.M., Kundinger, S.R., Wang, K., Williams, D., DeTure, M., Dickson, D.W., Cook, C.N., et al. (2020). Posttranslational Modifications Mediate the Structural Diversity of Tauopathy Strains. Cell *180*, 633-644.e12. 10.1016/j.cell.2020.01.027.

68. Pavlova, A., Cheng, C.-Y., Kinnebrew, M., Lew, J., Dahlquist, F.W., and Han, S. (2016). Protein structural and surface water rearrangement constitute major events in the earliest aggregation stages of tau. Proc. Natl. Acad. Sci. USA *113*, E127-136. 10.1073/pnas.1504415113.

69. Li, C.H., and Lee, C.K. (1993). Minimum cross entropy thresholding. Pattern Recogn. *26*, 617–625. 10.1016/0031-3203(93)90115-D.

70. Glasbey, C.A. (1993). An Analysis of Histogram-Based Thresholding Algorithms. CVGIP: Graph. Models Image Process. *55*, 532–537. 10.1006/cgip.1993.1040.

71. Hess, B., Kutzner, C., van der Spoel, D., and Lindahl, E. (2008). GROMACS 4: Algorithms for Highly Efficient, Load-Balanced, and Scalable Molecular Simulation. J. Chem. Theory Comput. *4*, 435–447. 10.1021/ct700301q.

72. Pronk, S., Páll, S., Schulz, R., Larsson, P., Bjelkmar, P., Apostolov, R., Shirts, M.R., Smith, J.C., Kasson, P.M., van der Spoel, D., et al. (2013). GROMACS 4.5: a high-throughput and highly parallel open source molecular simulation toolkit. Bioinformatics *29*, 845–854. 10.1093/bioinformatics/btt055.

73. Robustelli, P., Piana, S., and Shaw, D.E. (2018). Developing a molecular dynamics force field for both folded and disordered protein states. Proc. Natl. Acad. Sci. *115*. 10.1073/pnas.1800690115.

74. Nosé, S. (1984). A molecular dynamics method for simulations in the canonical ensemble. Mol. Phys. *52*, 255–268. 10.1080/00268978400101201.

75. Hoover, W.G. (1985). Canonical dynamics: Equilibrium phase-space distributions. Phys. Rev. A *31*, 1695–1697. 10.1103/PhysRevA.31.1695.

76. Essmann, U., Perera, L., Berkowitz, M.L., Darden, T., Lee, H., and Pedersen, L.G. (1995). A smooth particle mesh Ewald method. J. Chem. Phys. *103*, 8577–8593. 10.1063/1.470117.

77. Verlet, L. (1967). Computer “Experiments” on Classical Fluids. I. Thermodynamical Properties of Lennard-Jones Molecules. Phys. Rev. *159*, 98–103. 10.1103/PhysRev.159.98.

78. Hess, B., Bekker, H., Berendsen, H.J.C., and Fraaije, J.G.E.M. (1997). LINCS: A linear constraint solver for molecular simulations. J. Comput. Chem. *18*, 1463–1472. 10.1002/(SICI)1096-987X(199709)18:12<1463::AID-JCC4>3.0.CO;2-H.

79. Miyamoto, S., and Kollman, P.A. (1992). Settle: An analytical version of the SHAKE and RATTLE algorithm for rigid water models. J. Comput. Chem. *13*, 952–962. 10.1002/jcc.540130805.

80. C. Dallin, B., S. Kelkar, A., and Lehn, R.C.V. (2023). Structural features of interfacial water predict the hydrophobicity of chemically heterogeneous surfaces. Chem. Sci. *14*, 1308–1319. 10.1039/D2SC02856E.

81. Monroe, J.I., and Shell, M.S. (2019). Decoding signatures of structure, bulk thermodynamics, and solvation in three-body angle distributions of rigid water models. J. Chem. Phys. *151*, 094501. 10.1063/1.5111545.